aerospace

MDPI

*Article*

# Design and Analysis of a Baseline Fuel Cell Thermal Management System in a Conceptual Aircraft Design Framework

**Philip Balack *, Daniel Silberhorn, Tim Burschyk and Angel Garmilla Manzano**

German Aerospace Center (DLR), Institute of System Architectures in Aeronautics, 21129 Hamburg, Germany
* Correspondence: philip.balack@dlr.de

**Abstract**

Hydrogen-fueled fuel cell aircraft require powerful thermal management systems to operate. The sizing and integration of these systems remain a key challenge for this type of propulsion system. This study investigates the impact of a fuel cell cooling system on a parallel-hybrid regional aircraft by means of integrating a cooling system model within a conceptual aircraft design workflow. The workflow includes key design parameters of the fuel cell and the thermal management system for co-optimization towards minimum aircraft CO2 emissions. The multi-objective optimization of the thermal management system includes a ranking of drag, mass and power consumption impacts. The thermal management system drag is found to have the largest impact at aircraft level. It is most affected by the heat exchanger fin geometry and frontal area. A wide-ranging drag-specific heat rejection of 1.8 to 14 kW/N is observed for the clean-sheet aircraft design during cruise flight. Larger frontal areas and the implied substantial reduction in thermal management drag outperform the drag increase in larger fairings that contain the heat exchanger. It is also shown how the optimization of the fuel cell load and operating temperatures can minimize the system penalty. This highlights the need for an integrated design approach to reduce the system impact.

**Keywords:** fuel cell thermal management; hydrogen fuel cell; hybrid-electric aircraft; conceptual aircraft design

## 1. Introduction

Fuel cell-powered aircraft fueled by hydrogen have the potential to cut greenhouse gas emissions of regional aircraft. Not only the decarbonization of the flight operation but also the efficiency gain versus combustion engines in regional turboprop aircraft promote the adoption of hydrogen as fuel and fuel cells as means of energy conversion [1,2].

### *1.1. Background*

A drawback of today's most widely used proton-exchange membrane fuel cells is the low operating temperature of approximately 80 to 100 °C. The rejection of waste heat to the ambient air at small temperature differences requires substantial amounts of cooling airflow and considerable installation spaces for cooling systems on the airframe. The typical thermal management system (TMS) architecture discussed in the literature is a single-phase cooling medium transferring the bulk of the waste heat to the ambient air via a liquid-to-air heat exchanger [3–11]. One alternative for liquid coolants is a mechanically pumped liquid/vapour mixture [3,7]. Van Gerner et al. [7] indicate that such two-phase systems have been originally developed for space applications for reduced thermal management mass.

Check for updates

Academic Editor: Konstantinos Kontis

Received: 2 September 2026
Revised: 13 October 2026
Accepted: 15 October 2026
Published: 19 October 2026

**Copyright:** © 2026 by the authors. Licensee MDPI, Basel, Switzerland. This article is an open access article distributed under the terms and conditions of the Creative Commons Attribution (CC BY) license.

Quaium et al. [3] confirmed considerable mass reductions versus a liquid coolant. However, the two-phase system is more complex and its feasibility requires further evaluation [3,7]. An alternative to liquid-cooled stacks is the evaporative cooling technology from Intelligent Energy where coolant and cathode flow are combined [12]. This technology is being developed in UK-based projects to deliver fuel cell systems for commercial aircraft in the near future [12].

### 1.2. Research on Thermal Management System Impact

The thermal management system can be sized and optimized independently; however, interactions with the fuel cell system drive the total performance of the propulsion system at aircraft level and should be considered to achieve the best compromise. Several system-level studies have identified key design parameters that drive the multi-objective optimization of fuel cells and their accompanying thermal management systems. The impact on the aircraft is reflected in terms of system mass, efficiency, drag and volume. The main design parameters are the stack sizing, the fuel cell operating temperature and pressure, the liquid-to-air heat exchanger type and sizing as well as margins with respect to hot-day ambient temperatures. For instance, the stack sizing strongly impacts the trade-off between mass, efficiency and drag [5,6,11]. The stack sizing affects both the fuel cell and the thermal management system. The main heat exchanger, however, is sized to the coolant flow requirements of the stack and can largely be optimized independently. The heat exchanger properties such as frontal area and temperature effectiveness have been shown to critically impact the momentum drag of the cooling air [5,6].

Schröder et al. [5] point out that the propulsion system domains of mass, efficiency, volume and drag reflect contradicting optimization targets and a compromise must be found at aircraft level. Thus, aircraft design studies have included fuel cell thermal management models to address the impact on aircraft performance and in the best case traded thermal management design parameters. Nozinski et al. [13] integrated a detailed thermal management system model with higher-fidelity models of a full-electric fuel cell powertrain in a retro-fit type of aircraft performance analysis. The weight and flight performance of all powertrain components including the thermal management system is iterated, providing insights into re-sizing effects at the constraint of a fixed take-off mass, aircraft drag and payload reduction. The co-current optimization of multiple parts of the thermal management system is performed with a genetic algorithm. A sizing strategy towards heavy, but low-drag heat exchangers is identified as mission energy optimal. Eissele et al. [14] designed a clean-sheet regional aircraft with low-temperature fuel cells as single power source and a ram-air thermal management system. However, there the thermal management system mass and drag were re-scaled from another aircraft study which dealt with a larger aircraft size and very different top-level aircraft requirements.

Rischmüller et al. [10] designed a regional turboprop retro-fit with a high-temperature fuel cell and fan supported ram-air thermal management system in a low hybridization scenario. A dedicated model with a multi-objective optimization for mass, drag and power consumption was used to predict a range of TMS performances. The results were fed back to the aircraft design process as a surrogate model. Nicolosi et al. [15] performed trade-off studies on the thermal management design of a fuel cell-powered aircraft. Variations in input power of a puller fan and nozzle length were investigated to minimize the aircraft energy consumption of the clean-sheet aircraft design. Habrard et al. [8] designed a parallel-hybrid retro-fit of an 8-seater commuter aircraft with a low-temperature fuel cell which contributes power during cruise flight. A thermal management model was directly integrated in the aircraft design process to trade fuel cell stack sizing, operating temperature, ISA temperature margins and coolant variations. Furthermore, five different

offset-strip fin geometries were evaluated. Similar to the study from Rischmüller et al. [10], the trade-offs were evaluated with respect to aircraft CO2 emissions and payload reduction on the fixed aircraft. An overview of the discussed literature is given in Table 1.

**Table 1.** Literature on hybrid or full-electric PEM fuel cell aircraft and thermal management co-design.

| Reference | Aircraft Study Type | Architecture | TMS Method | External TMS Drag | TMS Trade-Offs/Optimization |
|---|---|---|---|---|---|
| Nozinski et al. [13] | Retro-fit | Full-electric LT-Fuel Cell | Integrated | Spillage | Heat exchanger internal geometry & effectiveness & tilting, diffusor area ratio |
| Eissele et al. [14] | Clean-sheet | Full-electric LT-Fuel Cell | Scaled Performance | No | None |
| Rischmüller et al. [10] | Retro-fit | Hybrid HT-Fuel Cell | Surrogate model | Fairing, spillage drag | Drag, mass & power optimization |
| Nicolosi et al. [15] | Clean-sheet | Full-electric LT-Fuel Cell | Integrated | Fairing drag | Fan power, nozzle length |
| Habrard et al. [8] | Retro-fit | Hybrid LT-Fuel Cell | Integrated | No | Heat exchanger internal geometry, coolant type & temperature |

### *1.3. Aim and Structure*

The research gap is identified as the integration of a thermal management system model in a clean-sheet aircraft design with sufficient parametrization to analyze the influence of various TMS design parameters on TMS weight, internal and external drag and aircraft emissions for a low-temperature fuel cell system that contributes significant power primarily in cruise flight. This specifically means that the heat exchanger is sized and optimized for cruise flight conditions. Clean-sheet and retro-fit design studies are separate applications and conclusions with respect to system design may not align due to different optimization objectives (e.g., the effect on available payload on a fixed aircraft). Furthermore, the impact of the thermal management system and its optimization depends on the propulsion architecture. The outcome may change between hybrid aircraft and those with a full-electric fuel cell power train.

In this study, the outlined research gap is addressed by integrating a thermal management system model in an aircraft design workflow. The workflow properly includes re-sizing effects of all lifting surfaces and the propulsion system. This allows the evaluation of design parameter variations in fuel cell heat exchanger size, stack sizing and operating temperature for an aircraft with fixed top-level aircraft requirements. As a baseline thermal management architecture, the present study deals with a single-phase liquid cooling system.

## 2. Aircraft Concept

The aircraft in this study is based on a concept from the Clean Aviation HERA project [16]. It is an 80-seater, twin-turboprop aircraft with a parallel-hybrid electric propulsion system. Two fuel cell systems are located below the cabin, in the centre of the fuselage, and support the gas turbines on the wing via electric motors mounted on power combining gearboxes (see Figure 1).

The gas turbines, as main power providers, are fueled by kerosene stored in wing tanks and operate from engine start-up to shut-off. Electrical generators on the gas turbines provide the required power for the all-electric on-board systems until the fuel cell is able to supply this power. The fuel cell starts to contribute power after take-off when sufficient ram-air pressure is available to reject the heat to the ambient.

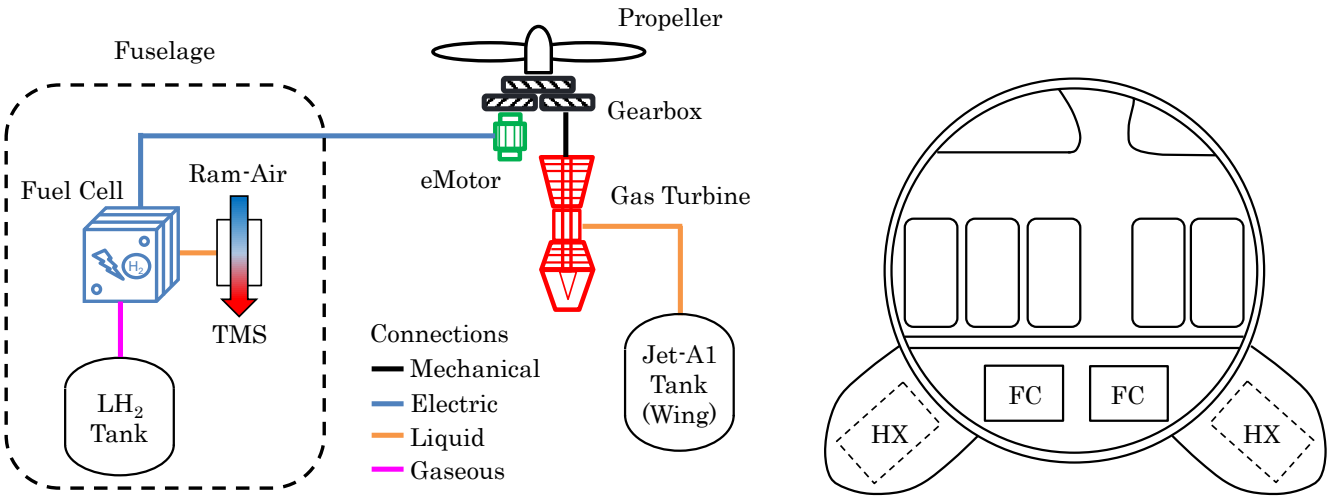



**Figure 1.** Schematic of the parallel-hybrid propulsion architecture on the left side with fuel tanks, fuel cells, fuel cell thermal management system (TMS), electric motor, gas turbine and power combining gearbox. The single $LH_2$ tank located behind the aft pressure bulkhead feeds both fuel cell systems. Right side: Sketch of the cross-section with the fuel cell system in the underfloor compartment and the heat exchangers in the landing gear fairing.

The fuel cell contributes between 70 and 80% to propeller power during cruise flight and supplies the all-electric on-board systems. The actual power share depends on the minimum rated gas turbine power as well as on the impact of the TMS. The gas turbines are running at least at idle power during cruise to prevent re-start issues. The two fuel cell systems are fueled by a single liquid hydrogen tank in the rear of the fuselage. The fuel tank capacity is fixed to 600 kg of liquid hydrogen. This is about 70% of what is required for the block and reserve mission fuels on the design mission. The unused volume provides room for increased range at reduced payload. The fuel cell TMS is integrated in the belly fairing in close proximity to the heat source. The design point of the TMS is defined at cruise flight for two reasons: Overall, the hydrogen fuel cell acts as a secondary power provider to substitute kerosene fuel energy consumption with minimum snow-ball effects. The gas turbine as main power provider makes up for additional required power in any other flight phase. The priority of the concept is to decarbonize the flight operation and not to optimize for lowest energy consumption versus a conventional aircraft. Figure 2 shows a visualization of the aircraft. Table 2 lists the various top-level aircraft requirements (TLAR) and key characteristics of the aircraft.

**Table 2.** Top-level aircraft requirements and key characteristics.

| Parameter | Unit | Value |
|---|---|---|
| Passenger Capacity | - | 80 |
| Design Range (ISA STD) | nmi | 500 |
| Evaluation Range (ISA + 10°C) | nmi | 250 |
| Cruise Mach number | - | 0.5 |
| Approach Speed | KTAS | 120 |
| Max. Operating Altitude | ft | 25,000 |
| Take-off Field Length (SL, ISA) | m | 1350 |
| Alternate Distance | nmi | 100 |
| Final Reserve | min | 30 |
| Wing Span Limit | m | <36 |
| Wing Aspect Ratio | - | 14 |
| LH2 Mass | kg | 600 |

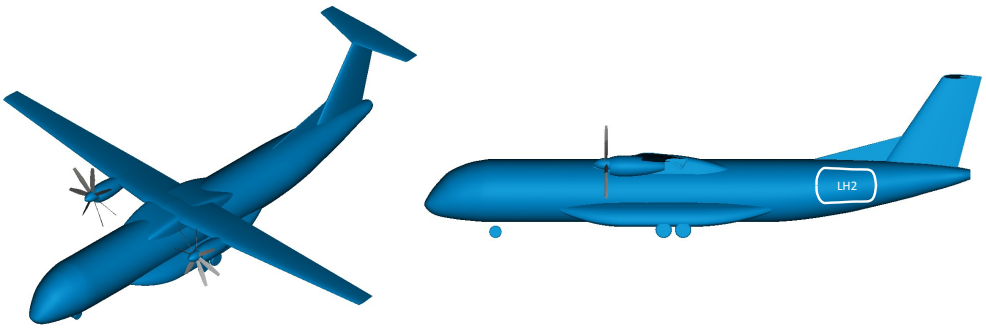



**Figure 2.** Visualized CPACS geometry of the aircraft concept.

## 3. Aircraft Design Workflow

Figure 3 shows a simplified flow chart of the iterative design workflow. The design starts with top-level aircraft requirements such as passenger capacity, design range, speed requirements, reserve mission rules, etc. Additional design parameters are also provided which include sizing rationale for the fuel cell stacks as well as optional increments to the ISA standard atmosphere temperature for the oversizing of the thermal management system. The conceptual design of the aircraft is performed with the tool openAD which generates an iterative solution of an aircraft description including geometry, weights and aerodynamic performance based on all the above inputs [17].

It receives updated input from the design loop on mission fuel, fuel cell system and TMS masses as well as a calibration for the propeller shaft power to match the required take-off field length (TOFL). The engine performance is a combination of lo-fi gas turbine, fuel cell and propeller models and the TMS performance. The gas turbine model comprises a physical, but simplified thermodynamic cycle calculation that is rubberized to the required sea-level output and computes the power output as well as the residual thrust for the whole operating envelope. It is based on the textbook from Bräunling [18].

The fuel cell performance is modelled with a linear relationship between efficiency and rated power at stack level. Altitude-dependent power consumption ratios for the auxiliary components (e.g., compressor, pumps) drive the net fuel cell output. The fuel cell model is based on simplified methods that require few input parameters, is easily adapted to a specific reference performance and allows design exploration with respect to the stack working point, i.e., the trade-off between system mass and efficiency. This makes it a good choice for the integration in an overall aircraft design workflow. The details of the model are provided in Appendix A. The weight and volume of the fuel cell system are estimated and fed back to openAD in the next iteration. However, practically, the volume of the fuel cell in the underfloor location is unconstrained; therefore, it has no effect on the result. The TMS model receives the required heat rejection for the design point as well as a map of operating points and heat loads of the fuel cell as input. The TMS performance limits the fuel cell power across all off-design conditions.

The propeller model is a lo-fi actuator-disk model with additional assumptions on blade friction drag that computes the propeller thrust based on the available shaft power range across the operating envelope. The propeller has a fixed diameter and blade count. The engine performance module takes the gas turbine map and combines it with the TMS limited fuel cell map to compute the available shaft power on the propeller. The minimum power is always the gas turbine idle power while the installed propeller shaft power is the upper limit. The propeller model inside the engine performance module is then used to compute the propeller thrust. The propeller and residual thrust of the gas turbine are combined with the TMS drag as the total thrust.

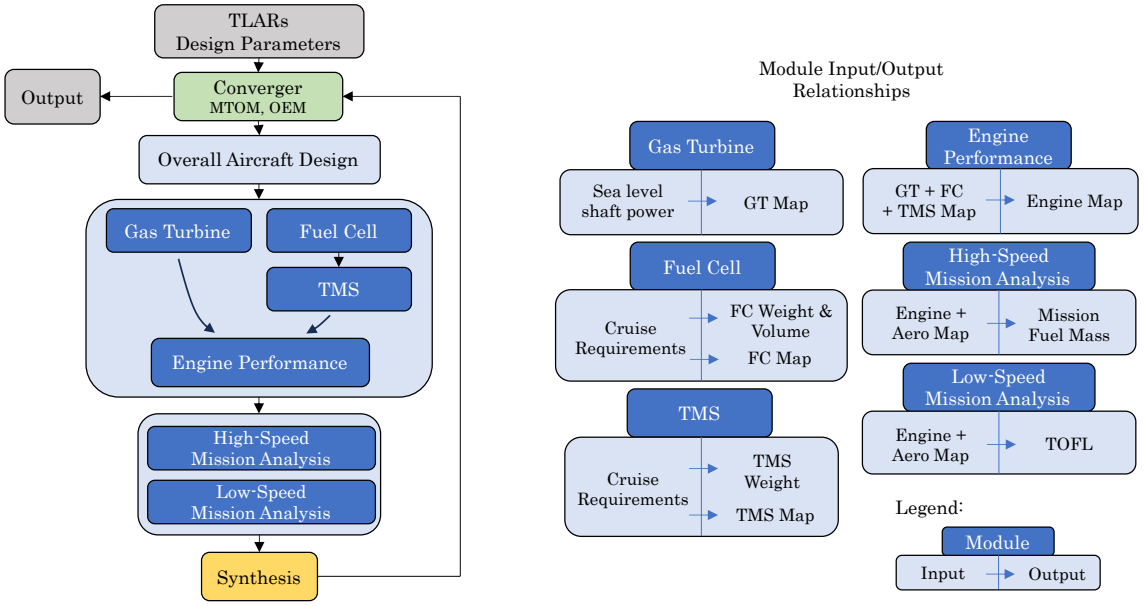



**Figure 3.** Convergence loop of the aircraft design workflow on the left side including the various disciplinary tools. The loop is driven until convergence of MTOM and OEM are both reached. The RCE software is used to connect the tools [19]. Each tool uses the CPACS data schema to exchange input and output information [20]. The main sizing inputs and tool outputs of each module in the workflow are listed in additional blocks on the right side.

The full engine map and the aero performance map from openAD are used in the subsequent high-speed mission analysis tool. This tool performs the time-step simulation of the aircraft as a point mass along the defined trajectory based on the 2D equations of motion. The output of this analysis is the block and reserve fuel burn (Jet-A1 + LH2) for the 500 nmi design mission. This is fed back to openAD in the next iteration. The take-off simulation is performed with the LSperfo tool which evaluates the achievable take-off field length with all operating cases including the one-engine inoperative case [21]. It is also based on a time-step simulation of the aircraft as a point mass on the take-off trajectory. This result is also fed back to openAD to re-size the propeller and gas turbine power. The design cycle is repeated until convergence of the maximum take-off mass (MTOM) and the operating empty mass (MOEM) is reached. Upon completion of the loop, two 250 nmi evaluation missions are computed, one on an ISA standard day and another on a "hot-day" with an ISA temperature increment of +10 °C. The speed schedule on these evaluation missions is unchanged versus the design mission.

All information is stored in the CPACS data format which is able to manage the multi-disciplinary, multi-fidelity process [20]. All CPACS tools are connected via the RCE tool integration environment [19].

## 4. Cooling System Model

This section covers the TMS model and its theoretical background. First, a technical overview of the system, its design parameters and the heat exchanger integration is given. This is followed by subsections on diffusor performance, heat transfer modelling, core pressure drop estimations, nozzle losses, mass estimation, design point optimization and off-design analysis. This is wrapped up by a section on the validation of the heat exchanger core. The methodology is based on the existing open literature. Deviations from other TMS models arise in the formulation of the design constraints such as the frontal area of the heat exchanger and how the optimization for lowest impact is conducted as well as in various aspects of the mass estimation such as for the coolant pump.

### *4.1. Overview*

The TMS architecture visualized in Figure 4 comprises a ram-air channel with diffusor, a heat exchanger and a nozzle. The nozzle is assumed to have a variable geometry to control the airflow in off-design conditions to minimize the cooling drag. The internal drag of the ram-air duct is computed as well as the spillage drag contribution.

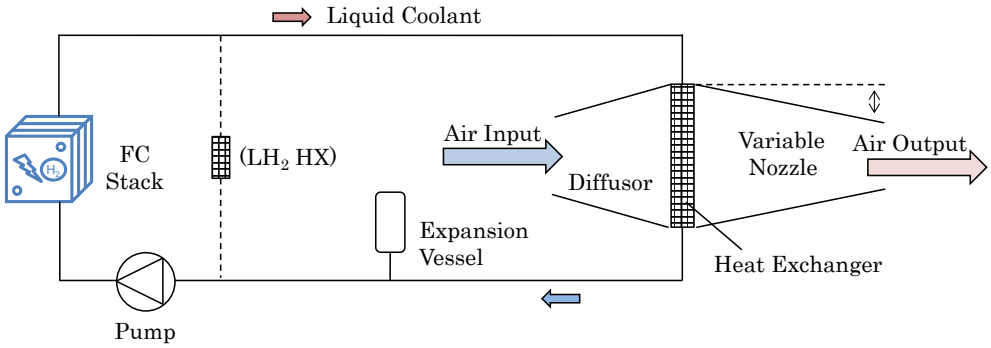



**Figure 4.** Liquid cooling loop with sketch of the ram-air channel with diffusor, liquid-to-air heat exchanger and nozzle.

The liquid hydrogen is assumed to be vaporized in an electrical heater based on the architecture proposed by Burschyk et al. [22]. However, leveraging the vaporized hydrogen as a heat sink for the fuel cell coolant absorbs approximately 4.2 MJ/kg which translates into about 7% of the generated heat. This is estimated with the enthalpy tables of the National Institute of Standards and Technology (NIST) based on the temperature increase in cold hydrogen to the fuel cell entry temperature of 80 °C [23]. The risk of coolant freezing is thereby neglected. The heat load that is discussed in the remaining sections of the paper is therefore the net portion that has to be dissipated through the liquid-to-air heat exchanger. The $LH_2$ heat exchanger is assumed to be placed in a parallel line to the liquid-to-air heat exchanger. This allows to minimize the coolant mass flow that has to travel the longer distance to the $LH_2$ heat exchanger which is placed close to the tank in the rear of the fuselage. The weight of this parallel line including the $LH_2$ heat exchanger and associated coolant pressure losses are not estimated. It is assumed that the overall impact is low. Figure 5 shows the outer dimensions and the flow arrangement of the heat exchanger.

The design parameters of the model are provided in Table 3. The frontal area of the heat exchanger is given as input. The heat exchanger aspect ratio is defined as

$$AR_{HX} = \frac{L_{stack}}{L_{liq}}. \tag{1}$$

The frontal area of the heat exchanger is given as input. The diffusor area ratio is the ratio of the heat exchanger free flow area to inlet throat area. Figure 4 shows the principle connections in the coolant network.

**Table 3.** Design parameters of the TMS model.

| Parameter | Symbol | Unit | Range |
|---|---|---|---|
| Design heat load | $\dot{Q}_d$ | kW | - |
| Frontal area | $A_{2_{tot}}$ | $m^2$ | - |
| Heat exchanger aspect ratio | $AR_{HX}$ | - | 1–5 |
| Coolant inlet temperature | $T_{liq,in}$ | °C | 80–95 °C |
| Coolant temperature drop | $\Delta T_{liq}$ | °C | <=10 °C |
| Temperature increment to ISA | $\Delta T_{ISA}$ | °C | - |
| Diffusor area ratio | $AR_{Dif}$ | - | 2–4 |

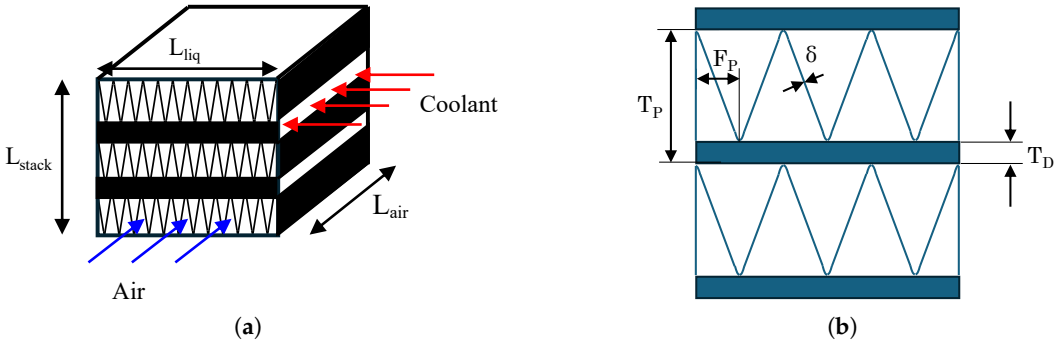



**Figure 5.** Layout of the louver fin heat exchanger with rectangular tubes in (**a**). Sketch of the air passage geometry in (**b**).

### *4.2. Heat Exchanger Integration*

The heat exchanger is integrated in the landing gear fairing. The principle arrangement is shown in Figure 6. As a preliminary assumption, the fuselage pressure hull is not to be penetrated by the heat exchanger and its upstream and downstream ducts. The heat exchanger is tilted against the flight direction at 70° in order to limit the belly fairing size. According to Nichols [24] tilting angles of up to 70° against the straight upstream incur a moderate increase in pressure drop.

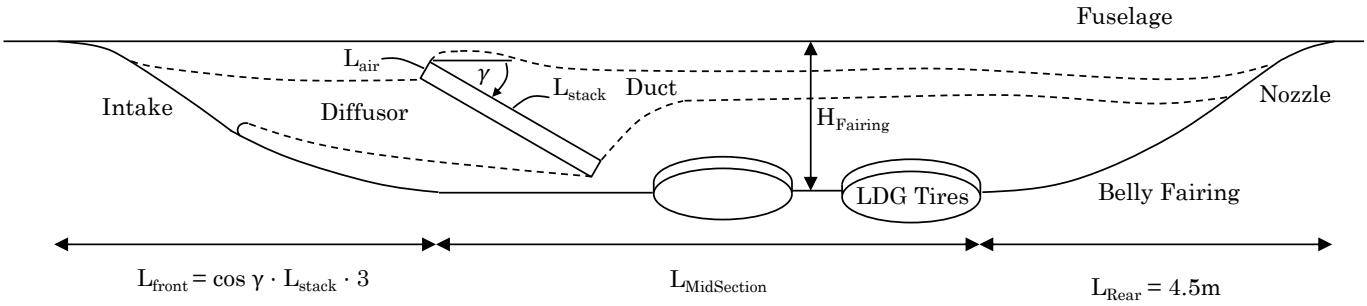



**Figure 6.** Principle heat exchanger integration in landing gear fairing.

The exact geometry of the intake, diffusor and ducts ahead of and past the heat exchanger is not defined. The effective tilt angle might be higher. However, as a preliminary assumption no additional pressure drop is considered. Likewise, no additional pressure drop is assumed for the downstream duct that extends through the fairing until the variable nozzle in the rear.

The fairing is split into three segments. The front segment length depends on the heat exchanger stack length and the tilt angle. The constant cross-section segment includes the tandem main landing gear tires and a forward margin for the heat exchanger. The rear segment is fixed at a length of 4.5 m. The constant cross-section plane is shown in Figure 7. The fairing height is defined as

$$H_{Fairing} = (cos\gamma \cdot L_{air}) \cdot 4 + sin\gamma \cdot L_{stack}. \quad (2)$$

The fairing width is estimated as the heat exchanger liquid flow length plus a margin of 0.5 m. The cross-section area in the mid-section is approximated with the profile geometry of the fairing. This is needed for the computation of the form factor $FF$ based on the method provided by Torenbeek [25]. This is then applied in the zero-lift drag estimation

$$CD_{0_{Fairing}} = \left(r_{lam} \cdot C_{f_{lam}} + (1 - r_{lam}) \cdot C_{f_{turb}}\right) \cdot A_{wet} \cdot (FF + Q - 1)/A_{ref}, \quad (3)$$

where $r_{lam}$ denotes the ratio of laminar flow length, $C_{f_{lam}}$ the laminar and $C_{f_{turb}}$ the turbulent friction coefficients, $A_{wet}$ the wetted and $A_{ref}$ the wing reference area. $Q$ denotes the drag penalty factor due to interference between fairing and fuselage. A ratio of 5% laminar flow length is set as well as an interference factor of 1.5. The fairing is lofted with the TiGl library [26] and the true wetted area is computed. The fuselage area that is shaded by the fairing is also computed with the TiGl library via boolean operations in order to correct the fuselage drag. The minimum fairing size is approximated as the one that includes the outer lateral landing gear position as shown in Figure 7.

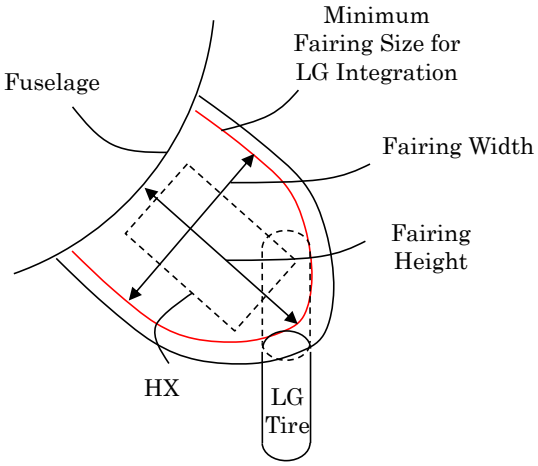



**Figure 7.** Front view of belly fairing cross-section examples with heat exchanger and landing gear integration (not to scale).

The belly fairing is a simplified shape but it scales with the heat exchanger size and therefore affects the total aircraft performance. In addition, the weight of the fairing is estimated with a specific weight of 7.5 kg/m$^2$. This specific weight is approximately 15% lower than what the method from Torenbeek [27] predicts. A technology-driven 15% weight reduction is considered because of the overall progress since the release of the book. The heat exchanger aspect ratio impacts the fairing cross-section. An aspect ratio of 3 is kept constant throughout the trade-offs. This value was found to give an acceptable initial alignment between the fairing sizing for landing gear integration and for the heat exchanger.

### *4.3. Diffusor Losses and Spillage Drag*

There are empirical correlations to estimate diffusor pressure drop which require input parameters such as area ratios, opening angles, etc. Often this information and the appropriate diffusor design is not available in the conceptual design phase. One way to account for losses is to use a relative total pressure drop invariant of mass flow as proposed in [6,28–30]. In those studies, the pressure ratio ranges from 96% to 99%. However, Kellermann et al. point out that in off-design conditions at lower mass flows this could lead to pessimistic results [31]. Pittaluga [32] developed a correlation for the estimation of the pressure rise in a "flat" two-dimensional diffusor. There, the diffusor exit pressure

$$p_{out} = c_p^* \cdot q_{in} + p_{in} \tag{4}$$

is correlated via the pressure coefficient $c_p^*$ based on the dynamic pressure at the inlet. This coefficient is sensitive to the diffusor area ratio, the inlet Mach number, Reynolds number and the aspect ratio of the inlet plane as well as the inlet blockage. The correlation is valid up to inlet Mach numbers of Ma 0.8. The Mach numbers occurring in the present application are well below this threshold. The reader is referred to the source for the rather complex definition of $c_p^*$ [32]. The recommended diffusor area ratios to be evaluated range between

two and four. The pressure recovery is very sensitive to the inlet blockage. The lowest value according to the correlated range was selected (i.e., 0.02), assuming the best-case scenario. Pittaluga [32] did not clearly state the length of the correlated diffusors. It is assumed that any typical diffusor opening angle is covered with the margins in fairing length.

At part load, when less airflow is moving through the duct, spillage drag adds to the internal momentum drag. According to Malan et al. [33], it is common practice to estimate the spillage drag as a function of the theoretical additive drag as

$$D_{spillage} = K_{add} \cdot D_{add} \tag{5}$$

where

$$D_{add} = \dot{m}_{air} \cdot (v_{in} - v_{\infty}) + A_{in} \cdot (p_{in} - p_{\infty}). \tag{6}$$

Here the suffix "*in*" denotes the condition at the diffusor throat area. Additive drag is "the force exerted in the thrust direction on the streamtube of air entering the inlet of an air-breathing engine by the surrounding atmosphere" [34]. Additive drag is partially compensated by the suction force of the pressure distribution on the intake cowling. The factor $K_{add}$ expresses this drag reduction. The value of $K_{add}$ depends on cowl geometry, mass flow ratio ($MFR$) and Mach number [33]. Mount performed experiments on NACA type inlet geometries typically used on fast subsonic and supersonic aircraft engine intakes to correlate this reduction factor [34]. The experiments were conducted at flight Mach numbers 0.3, 0.6, 0.9 and 1.27. There, the type E geometry performs well against other shapes with smaller lip radii and less contouring. According to the data, the $K$ factor becomes more and more relevant at lower mass flow ratios. At high mass flow ratios above 0.6, it is almost zero. It is assumed that a "good" intake design for the hybrid-electric aircraft would perform similarly. The type E behaviour tested at Mach 0.6 is used in the present study to correct the additive drag for all flight Mach numbers. It shows slightly higher $K$ factors compared to the case at Mach 0.3 and can thus be considered rather conservative. Therefore $K_{add}$ is computed as

$$K_{add} = -0.875 \cdot MFR + 0.625 \qquad \text{for } MFR \leq 0.6 \tag{7}$$

$$K_{add} = 0.1 \qquad \text{for } MFR > 0.6. \tag{8}$$

The diffusor losses and the spillage drag follow opposite trends. The smaller the intake area, the higher the internal diffusion losses, and the smaller the spillage drag and vice versa.

### *4.4. Heat Transfer Model*

The heat transfer model is based on the textbooks of Hesselgreaves et al. [35], Shah et al. [36] and VDI Heat Atlas [37]. The selected heat exchanger core type is a single-pass, cross-flow, louvered-fin, aluminum compact heat exchanger. The selected coolant type is a water-glycol mixture intended for use in fuel cells [38]. Subsequently a brief overview of the sizing methodology is provided. More details of the procedure are documented in Appendix B.

The sizing is based on the effectiveness-NTU method. The heat flow of the liquid and air stream

$$\dot{Q} = \dot{m}_{air} c_{p,air} \Delta T_{air} = \dot{m}_{liq} c_{p,liq} \Delta T_{liq}, \tag{9}$$

where $\dot{m}$, $c_p$, and $\Delta T$ are the respective mass flow, the specific heat capacity and the terminal temperature difference in each stream must be in balance. The maximum heat to be rejected is

$$\dot{Q}_{max} = C_{min} \cdot (T_{liq,in} - T_{air,in}), \tag{10}$$

with the minimum heat capacity

$$C_{min} = min(c_{p,air} \cdot \dot{m_{air}}, c_{p,liq} \cdot \dot{m_{liq}}). \tag{11}$$

The thermodynamic properties of the air at the entry are given by the flight speed, the required mass flow, pressure losses in the diffusor and the free flow area. The free flow cross-section area of the air is determined based on the core geometry configuration. The heat transfer effectiveness is then defined as

$$\epsilon = \frac{\dot{Q}}{\dot{Q}_{max}}. \tag{12}$$

The effectiveness is not to be confused with efficiency. The effectiveness indicates the ratio of actual heat transfer to the theoretical limit. This limit equals the air stream outlet reaching the inlet temperature of the coolant, which is not feasible and would require an infinitely long heat exchanger. A higher effectiveness means a higher outlet air temperature and consequently a lower air mass flow to absorb the same heat load. For a fixed heat exchanger frontal area, this translates into a longer core and therefore larger mass. The relationship between effectiveness, overall number of transfer units and heat capacity ratio of a cross-flow heat exchanger with both sides unmixed

$$\epsilon = 1 - exp\left(\left[exp(-NTU^{0.78} \cdot C^*) - 1\right] \cdot \frac{NTU^{0.22}}{C^*}\right) \tag{13}$$

is given in [35]. $NTU$ is the number of overall heat transfer units and

$$C^* = \frac{C_{min}}{C_{max}} = \frac{min(c_{p,air} \cdot \dot{m}_{air}, c_{p,liq} \cdot \dot{m}_{liq})}{max(c_{p,air} \cdot \dot{m}_{air}, c_{p,liq} \cdot \dot{m}_{liq})} \tag{14}$$

is the ratio of minimum and maximum heat capacity. The air side temperature increase, i.e., the effectiveness, is optimized based on the method presented in Section 4.9. Any plausible value of $\Delta T_{air}$ is tested in the model and the results are stored. However, not every value yields a convergence for the heat balance and the $NTU$ approximation. The lower end of the temperature delta, i.e., the highest air mass flow, is constrained by the requirement that the ratio of upstream capture area and inlet throat area does not exceed unity. The liquid side temperature drop $\Delta T_{liq}$ is an input parameter. The relationship between total, air and liquid side transfer units is given in [35] as

$$\frac{1}{NTU} = \frac{1}{N_{air}(C_{air}/C_{min})} + \frac{1}{N_{liq}(C_{liq}/C_{min})}, \tag{15}$$

where the wall resistance and hot and cold side fouling resistances are neglected. The determination of the air side and liquid side transfer units requires the computation of several physical properties. The air flow length is a result of this procedure. For a detailed view the reader is referred to Appendix B. Among the required physical properties is the non-dimensional heat transfer performance via the Colburn factor $j$. This heat transfer performance depends on the specific geometry of the heat exchanger core. Similar to Schröder et al., corrugated louvered-fin heat exchanger core geometries (type A with triangular channels and type C with rectangular channels) from the Chang database in [39] have been used in this study.

Chang et al. [39] present two correlations for the air side Colburn factor: A simple one that is only sensitive to louver pitch Reynolds number $Re_{air_{Lp}}$ and an expanded one that is sensitive to Reynolds number and a wide range of geometric input parameters

(validity range of both correlations: $100 < Re_{air_{Lp}} < 3000$). The present model includes both correlations but the expanded one is preferred and was used primarily for the results of this paper. The expanded one correlates 89.3% of the corrugated louver fin data within ±15% and has a mean deviation of 7.55% [39]. Their respective impact on the performance has been evaluated for a few selected core geometries of the Chang database in Appendix D.

### *4.5. Heat Exchanger Pressure Drop*

The air pressure drop in the heat exchanger is computed based on the core mass velocity approach. According to Chang et al. the pressure drop estimation

$$\Delta p = \frac{G_c^2}{2\rho_{in}}\left[(1-\sigma^2+K_c)+2\left(\frac{\rho_{in}}{\rho_{out}}-1\right)+f\frac{4L}{d_{h_{air}}}\frac{\rho_{in}}{\rho_m}-(1-\sigma^2-K_e)\frac{\rho_{in}}{\rho_{out}}\right], \quad (16)$$

is composed of several terms that consider the compression losses at the entry, the losses due to momentum change, the friction losses and the losses incurred by rapid expansion at the exit. In accordance with [36,40], the coefficients $K_c$ and $K_e$ are obtained from the respective curves at $Re_\infty$. The mass velocity $G_c$ is defined as the ratio of the air mass flow and the air side free-flow area of the core $\dot{m}_{air}/A_0$. See Appendix B for the definition of the hydraulic diameter. The parameter $\sigma$ denotes the ratio of free-flow area to heat exchanger frontal area [36]. The Fanning friction factor $f$ is estimated with the correlation presented in [40]. The correlation yields an accuracy of ±15% for 83.14% of the data and a mean deviation of 9.21% (validity range: $150 < Re_{air_{Lp}} < 5000$). Similar to the heat transfer correlation, the friction correlation requires a wide range of geometric input parameters as well as the louver-pitch-based Reynolds number. For the definition of all geometry parameters, the reader is referred to the original source [40].

### *4.6. Coolant Pressure Drop*

The liquid side pressure drop estimation in the heat exchanger and in the piping is based on a mix of the Hagen–Poiseuille and the Blasius relationships as well as the friction correlation from Nikuradse. The equations are given in Appendix E. Based on typical values, the pump including the electric motor that moves the liquid in the system is assumed to have an efficiency of 65% [41]. The pump power is computed as

$$P_{Pump} = \frac{\Delta p \cdot \dot{V}}{\eta_p}. \quad (17)$$

The fuel cell stack in the coolant loop is assumed to cause a pressure drop of 0.3 bar. Valves, turns and other flow control devices are assumed to add 0.2 bar pressure drop. The diameter of the main coolant piping between fuel cell and heat exchanger is sized such that a total pressure drop of 2 bar is not exceeded. This assumption is based on the works of [5,7]. These fixed assumptions are also valid for off-design conditions as heat rejection is assumed to be controlled with a constant coolant mass flow. Therefore, the terminal temperature difference in the coolant needs to decline at part load. Pressure losses due to contraction and expansion in the headers of the heat exchanger are assumed to be negligible [36].

### *4.7. Nozzle Pressure Drop*

Some TMS studies rely on correlations from turbomachinery or gas turbine literature to estimate the losses [28,31]. Others take fixed assumptions on the adiabatic or isentropic nozzle efficiency [5,42]. Again, some authors assume a constant total pressure ratio, e.g., Kozulovic et al. [30]. Overall, the nozzle pressure losses should have the lowest impact on the TMS drag as the air experiences a favourable pressure gradient. In this study, it is

also assumed that a total pressure ratio of 99% sufficiently covers any applicable nozzle design. The basic concept is a convergent nozzle that has a variable throat area to match the required mass flow according to the heat transfer needs. This mechanism allows to substantially cut the drag versus a fixed nozzle. In the model, it is assumed that the exit flow is always discharged at ambient pressure.

### 4.8. Mass Estimation

The system mass comprises the dry mass of the heat exchanger, the coolant mass, the piping mass and the pump mass. The dry mass of the heat exchanger is estimated via the geometrically defined porosities of the air and liquid side. The geometry is derived in Appendix C. A 20% mass markup is assumed for the coolant headers. The coolant mass estimation includes the volume inside the fuel cell stacks, the heat exchanger, the pipes and the expansion vessel. The one-way distance between the stacks and the heat exchanger is roughly estimated at 3 m. The equivalent pipe flow length is estimated by doubling the one-way distance and multiplying with a factor of 1.5 for the consideration of turns. The coolant volume in the fuel cell stacks is considered by an assumption that 10% of stack volume is filled by the coolant. The additional reservoir volume required for expansion and contraction of the liquid amounts to about 6% at an operating temperature of 80 °C. A bottom temperature of −30 °C for contraction is assumed based on the limits of the coolant [38]. No additional coolant volume is assumed for transient operation. Likewise, no specific mass budget is allocated for the small reservoir vessel structure. Computing the minimum wall thicknesses with conventional methods for pressurized vessels gives negligible structural masses. This is in line with the assumptions from van Gerner et al. [7]. However, there might be additional systems necessary to control the reservoir, which are neglected in the present study.

The aluminum pipe mass is determined based on the minimum wall thickness recommended by the SAE installation manual for aircraft fuel and oil lines [43]. This was assumed to provide a reasonable first estimate of the structure. The equivalent pipe diameter described above is used for the calculation of the pipe mass. In addition, a factor of 1.5 on the resulting mass is considered for the presence of valves. Overall, the pipe mass estimated with this approach ends up being small, which is in part due to the proximity of the fuel cell to the heat exchanger. Pump mass estimations for fuel cell cooling systems vary to a large extent in the literature. A comparison of four correlations is made in Appendix F. A new correlation is derived for the present study as reported in Appendix F. Two pumps are assumed for redundancy purposes. A markup of 10% on the total TMS mass is assumed for miscellaneous masses and installation.

### 4.9. Heat Exchanger Effectiveness Selection

For each design requirement, a range of design heat exchanger effectivenesses is available to choose from. The selection follows a normalized approach which scores the penalties of drag, power and mass based on pre-defined reference values and weighting factors. Each domain is thought to add a relative amount of energy consumption to the aircraft. Simply speaking, 10% additional aircraft drag is assumed to add 10% of energy consumption; likewise, x% added take-off mass or y% of power consumption acts the same way. This normalization gives a comprehensible impression of the impact of a domain and also helps to compare the domains to each other.

The TMS effects on cruise flight performance best reflect the impact on mission level; it is therefore chosen as reference point for the TMS drag and power consumption. In this application, the TMS design point and cruise flight coincide. In other cases, the TMS would be sized for the critical requirement (e.g., take-off) but evaluated in cruise flight nonetheless.

The reference drag is selected to be the total aircraft mid-cruise drag excluding the TMS drag. The TMS drag is included in the engine performance and not under the regular aircraft drag polar since it is throttle dependent. The reference power is chosen to be the total cruise propeller shaft power. The reference mass is the maximum take-off mass.

Mission energy consumption may not scale one-to-one with additional cruise drag and power consumption or added mass. The time-dependent influence of the other flight phases can be considered by means of weighting factors. The normalized summarized penalty of the system, i.e., the objective value to be minimized, is

$$\Phi_{Total} = K_{Drag} \cdot \frac{D_{TMS}}{D_{Ref}} + K_{Power} \cdot \frac{P_{TMS}}{P_{Ref}} + K_{Mass} \cdot \frac{m_{TMS}}{m_{Ref}} \tag{18}$$

and in shorter form

$$\Phi_{Total} = \Phi_{Drag} + \Phi_{Power} + \Phi_{Mass}. \tag{19}$$

The weighting factors $K_{Drag}$, $K_{Power}$ and $K_{Mass}$ are fixed inputs in a workflow run. Figure 8 shows the design point optimization with each penalty contribution for the base case example. Drag and mass scale differently with effectiveness. The power consumption is constant due to the fixed coolant mass flow rate and target pressure drop. The applied weighting factors are based on a previously performed aircraft level sensitivity study for a regional turboprop with a similar capacity and design range. They amount to 0.9 for the drag, 0.9 for the power and 0.8 for the mass impact. The reference values $D_{Ref}$, $P_{Ref}$ and $m_{Ref}$ are updated every run of the aircraft workflow iteration. Overall, the effectiveness selection can be considered a pre-optimization at system level. A sensitivity analysis on the weighting factors is reported in Section 5.6.

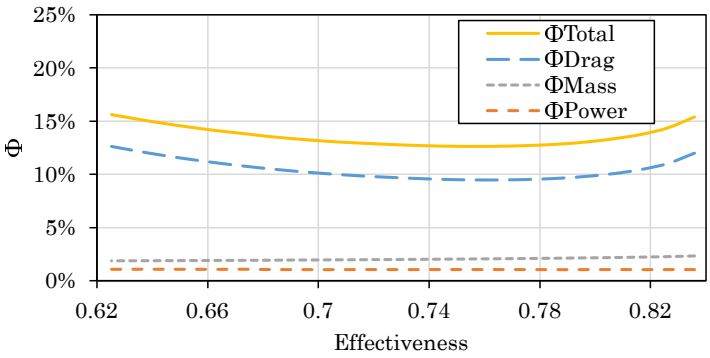



**Figure 8.** Example of available design space with respect to effectiveness. Each design is attributed with a summation of penalty scores of estimated aircraft impact in terms of drag, mass and power consumption.

### *4.10. Off-Design Analysis*

The design point calculation determines the heat exchanger length and therefore the heat transfer area. The model is able to compute the off-design TMS performance for a map of input conditions, i.e., coolant inflow temperature, heat load, altitudes, speeds and temperature increments to the ISA standard atmosphere model. The off-design routine iterates the air mass flow in order to fulfil the effectiveness-NTU relationships. The overall resistance of the heat transfer is given in [36] as

$$\frac{1}{UA} = \frac{1}{(\eta_0 \alpha A)_{air}} + \frac{1}{(\alpha A)_{liq}}, \tag{20}$$

where the wall resistance is neglected. See Appendix B for the definition of the surface effectiveness $\eta_0$ and for the definition of the heat transfer coefficient $\alpha$. The overall number

of transfer units is related to the product of overall heat transfer coefficient $U$ and total surface area by

$$NTU = UA/C_{min}. \quad (21)$$

With Equations (12) and (13), the actual cooling power and the air side terminal temperature difference are then determined. This process is iterated until all fluid properties are converged. The variable nozzle geometry is implemented such that the exit area matches the air mass flow required for the heat transfer. If the total pressure at the nozzle exit falls below ambient pressure, the operating point is neglected. The same applies if the mass flow ratio at the intake exceeds unity since expansion upstream of the intake is considered unfeasible with a ram-air system.

### 4.11. Heat Exchanger Plausibility Check

To the knowledge of the authors, there is no publicly available test data of a MW-level fuel cell heat exchanger (be it louvered-fin or other types). A plausibility check of the heat exchanger model was conducted with test data of a DLR fuel cell powertrain which was assembled in 2016 [44]. The tested heat exchanger was rated at 63 kW cooling power and was built with a herringbone fin type. Schröder et al. [5] reported the main characteristics. In the present work, two geometry configurations from the Chang database were selected, updated with increased fin and tube thicknesses and modelled at the test conditions. Aligning the heat exchanger pressure drop at the rated cooling air flow and heat rejection of the test heat exchanger requires at least a 50% larger heat exchanger volume. However, the reduction in pressure drop with reduced air flow is in good agreement. Large differences in performance may be attributed to the herringbone fin type. Due to confidentiality reasons not all the data can be provided here. The configuration 89 (see Table A1) was set as the baseline for the trade-off studies to serve as a conservative reference. The effect of the two different geometry configurations on TMS performance is discussed in Section 5.2. An optimization of the geometry for lowest pressure drop is theoretically possible with the correlations provided by Chang et al. in [39,40]. However, without back-up from applicable experimental data in the MW-level range or hi-fi analysis this is not considered useful at this point.

## 5. Results

In this section the workflow is applied to the design problem. First, a baseline TMS configuration is established and relevant inputs and outputs are reported. Afterwards variations in the core geometry are explored in order to highlight the sensitivity of the model to it. Furthermore, a sensitivity analysis of the diffusor performance is conducted. This is followed up by a preliminary system-level analysis to inform which design parameters have the largest impact. Further sensitivity studies for design parameters such as heat exchanger frontal area, stack oversizing and fuel cell operating temperature performed with the workflow conclude the analysis.

### 5.1. Baseline Configuration

The baseline configuration is defined as a heat exchanger with minimum frontal area, no stack oversizing and 80 °C fuel cell operating temperature. The design point heat load amounts to 1719 kW per heat exchanger to be dissipated at flight level 250 at a flight speed of Mach 0.5. The temperature increment to the ISA standard-day atmosphere model is set to +10 °C to allow the aircraft to fly without power constraints on warmer days. The frontal area of the heat exchanger is an iterative solution of the minimum viable area. The heat exchanger area is 25% larger than what would be required to integrate the main landing gear in the fairing (see Figure 7). The coolant temperature drop in the heat exchanger is

set to 8 °C. The diffusor area ratio is set at 3 and kept constant for all subsequent trade-offs. Table 4 lists a few output parameters and the weight breakdown for the TMS design point (ISA + 10 °C). On a standard-day mission the aircraft achieves a lift-to-drag ratio of 15.73 in cruise flight. This excludes the TMS drag since the TMS is accounted under the engine thrust. The TMS drag amounts to 960 N which is less than half of the design point drag. This highlights how much the ambient temperature affects the TMS performance. In standard-day cruise flight the total TMS drag makes up 10% of the aircraft drag (excl. TMS drag) and the belly fairing 8.2%. The block fuel consumption of the aircraft on the 500 nmi design mission amounts to 730 kg of Jet-A1 fuel and 319 kg of hydrogen.

**Table 4.** Output for the baseline TMS design point per engine (ISA + 10 °C).

| Parameter | Value | Mass Item | Weight Share |
|---|---|---|---|
| Frontal area | 1.21 $m^2$ | Pumps | 34% |
| HX air flow length | 14.6 cm | Fluid | 28% |
| TMS drag | 2200 N | HX Dry | 26% |
| Pump power | 17.6 kW | Miscellaneous | 9% |
| Mach HX Inlet | 0.143 | Pipes | 3% |
| Air mass flow | 25.13 kg/s | | |
| Coolant mass flow | 60 kg/s | | |
| Total pressure ratio diffusor | 97.9% | | |
| Heat exchanger air pressure drop | 5.15 kPa | | |
| Total pressure ratio TMS | 86.6% | | |

The total mass amounts to 341 kg which equals a specific heat rejection of 5.04 kW/kg. The pump mass makes up the dominant portion followed by the fluid mass and then the dry heat exchanger mass. The piping mass accounts for only 3% of the TMS mass.

Figure 9a shows the standard-day flight profiles of the baseline configuration per engine for total and fuel cell power in (a), fuel cell stack and net power and heat rejection in (b) and drag composition in (c).

The shown trajectory starts after take-off at 1500ft altitude at climb speed. The fuel cell system supplies a constant amount of power to the gear box and the on-board systems throughout the climb up to cruise. However, the stack output and thus heat load is increasing during climb because the air supply system requires more power at higher altitudes. The lower heat load at the beginning of the climb still comes at the largest drag penalty. With increasing true air speed and altitude, the TMS drag quickly drops whilst increasing the heat rejection during the climb. The spillage drag is negligible in climb and cruise as those are high-power phases with high mass flow ratios. In the low-power descent, the spillage drag equals the total TMS drag. In this segment the heat load is very low and the energized, heated air compensates the pressure losses.

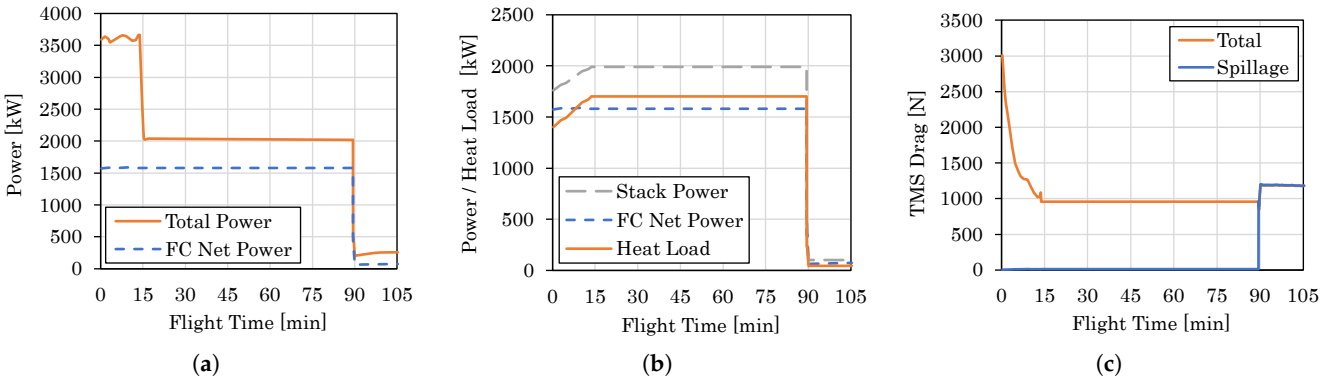



**Figure 9.** Flight profiles of the baseline at ISA standard-day temperatures. Fuel cell net power and total power per engine (fuel cell + gas turbine) in (**a**). Fuel cell power and rejected heat load by the heat exchanger per engine in (**b**). Total and spillage drag profile in (**c**).

### *5.2. Core Geometry Configuration Sensitivity*

Before looking at other system trade-offs, it is worth understanding the impact of different fin geometry configurations on heat exchanger performance. In the following example a comparison is made that excludes the pressure losses from diffusor and nozzle to enable a view on the heat exchanger contribution to drag. Figure 10a shows the pressure drop over the heat exchanger core and the internal momentum drag for the different original geometry configurations from the database. The differences relate to the louver pitch, angle and the fin pitch, thickness, height and tube diameter. The spread in pressure drop amounts to about 30% and in drag to about 80% between the worst and the best configuration, respectively. This shows the major impact that a specific set of geometries is estimated to have on the performance. Figure 10b shows the same configurations but with adaptations to the fin thickness and tube diameter. The original fin thickness for most of the configurations ranges between 0.04 mm and 0.07 mm and the tube diameter at 1.3 mm which was considered too thin for the aerospace application. A minimum value of 0.15 mm fin thickness and 1.5 mm tube diameter was set in line with [7]. Some of the configurations' performances are only slightly affected (i.e., 7–21) but some can even become applicable (60 and 61) which was not possible before because of excessive pressure drops. The configurations 85–90 improve in performance, especially 90 where a 40% reduction in pressure drop and a 65% reduction in drag is estimated. In this set of configurations the spread of the drag even exceeds 300% between the worst and the best. The effect on mass among the different configurations amounts to less than 15% deviation in mass specific heat rejection at total TMS level. Therefore, no strong correlation between heat exchanger drag and mass can be observed.

It is important to note that in this example the effectiveness for each configuration is optimized. Therefore the same pressure drop can result in a different drag for another effectiveness. However, this effect on drag was isolated with a separate tool run with fixed effectiveness. There it was observed that a relative change in pressure drop is doubled in its relative effect on internal drag.

Integrated in the aircraft design workflow including all other TMS losses i.e., diffusor, nozzle and spillage, the configuration 90 cuts the total TMS cruise drag by −40% versus the baseline (configuration 89). This results in a Jet-A1 fuel reduction on the standard-day design mission of −7.3%. For the 'hot-day' evaluation mission (250 nmi, ISA + 10 °C) with reduced range at constant maximum payload the aircraft requires 7.9% less Jet-A1 fuel. There the total TMS cruise drag during is cut by a similar magnitude of −39%.

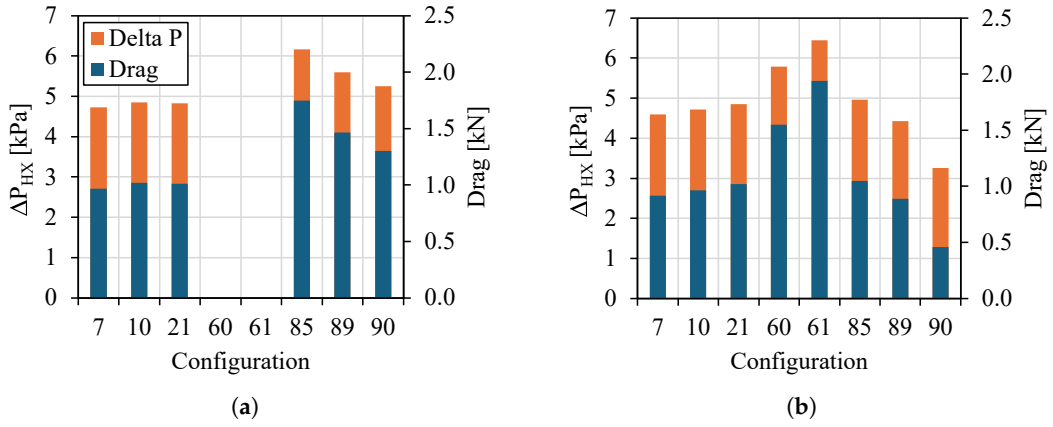



**Figure 10.** (**a**) Heat exchanger pressure drop and drag of various configurations with the original geometry from the database. (**b**) Heat exchanger pressure drop and drag of the configurations with geometry adaptation.

The results above emphasize how sensitive the heat exchanger performance estimation behaves with respect to apparently small geometry changes. This brings up the methodological challenge with respect to thermal management and conceptual aircraft design. The goal is to estimate not only the drag but ideally the exact dimensions and weight of the heat exchanger in order to perform space allocation and integration studies. This way, a better prediction of unconventional fuel cell aircraft performance is accomplished compared to typical 'guesstimates' used in conceptual design. However, heat exchanger performance analysis quickly requires a lot of detailed geometric inputs and thermodynamic calculations which can give a wide range of results that have a big impact. This is unusual for conceptual design where few and well-known top-level parameters are typically sufficient to describe a physical phenomenon (e.g., the lift-induced drag estimation requires only wing aspect ratio and Oswald factor). This underlines the importance of back-up from applicable test data or higher-fidelity analysis to improve the confidence in the heat transfer and friction correlations.

### *5.3. Diffusor Sensitivity Analysis*

The impact of a variable diffusor pressure recovery was evaluated in a small sensitivity study. The performance was varied by changing the blockage parameter within its correlated range at constant diffusor area ratio. The baseline blockage is set at 2%. A higher blockage results in a lower total pressure ratio of the diffusor (see Table 5). The higher diffusor total pressure drop at 6% blockage makes the baseline heat exchanger frontal area unfeasible as the nozzle outlet pressure would become sub-ambient. A larger frontal area with a lower heat exchanger pressure drop is required to cope with the decreased diffusor efficiency. The larger heat exchanger offsets the penalty and a similar outcome in Jet-A1 fuel is observed. However, further increasing the blockage to the maximum of 12% leads to a fuel penalty of 3.3% and a reduction in diffusor total pressure ratio by 1.9 percentage points versus the baseline. This shows that each percentage point in diffusor total pressure drop has a considerable impact on the result.

**Table 5.** Diffusor sensitivity analysis. The diffusor total pressure ratio is given at the design point conditions (DP) and at standard-day design mission cruise.

| Heat exchanger configuration | 89 | 89 | 89 | 90 |
|---|---|---|---|---|
| Diffusor blockage | 2% | 6% | 12% | 12% |
| Heat exchanger frontal area | 1.21 $m^2$ | 1.26 $m^2$ | 1.26 $m^2$ | 1.21 $m^2$ |
| Diffusor total pressure ratio (DP) | 97.9% | 97% | 96% | 95.6% |
| Diffusor total pressure ratio (DM) | 98.7% | 98% | 97.3% | 97.1% |
| Delta TMS cruise drag (DM) | - | +1.3% | +16.6% | −6.3% |
| Delta Jet-A1 fuel (DM) | - | +0.4% | +3.3% | −1.2% |

This is compared with the heat exchanger configuration 90 at maximum diffusor blockage and with baseline heat exchanger frontal area. The design point and cruise diffusor pressure recovery are the worst for this setting. Yet, the superior efficiency of the heat exchanger configuration offsets the diffusor penalty and still gives a reduction in Jet-A1 fuel consumption versus the baseline of −1.2%.

### *5.4. System-Level Sensitivities*

Another system-level sensitivity analysis for different cooling requirements has been performed for the heat exchanger frontal area, aspect ratio and liquid temperature drop. This helps to anticipate which trade-offs are most relevant to the aircraft level. Figure 11 illustrates the impact of each design variable on system mass, power consumption, and drag. The reference heat exchanger frontal area in this example is 1.3 $m^2$, the coolant temperature

drop 8 °C and the heat exchanger aspect ratio 3. The reference frontal area was selected this large to allow a deviation in both directions. The largest sensitivities to observe are the drag variations due to changes in frontal area or coolant temperature drop, and the sensitivity of system power to changing coolant temperature drop. The exponential impact of increased area, i.e., slower air velocity, on pressure drop is clearly indicated in Equation (16). The increased drag caused by a higher coolant temperature drop in the heat exchanger outweighs the reduction in pumping power at the aircraft level. The system mass is rather insensitive to any of the performed trade-offs. These sensitivities show the dominant influence of the frontal area and its relevance to the aircraft level.

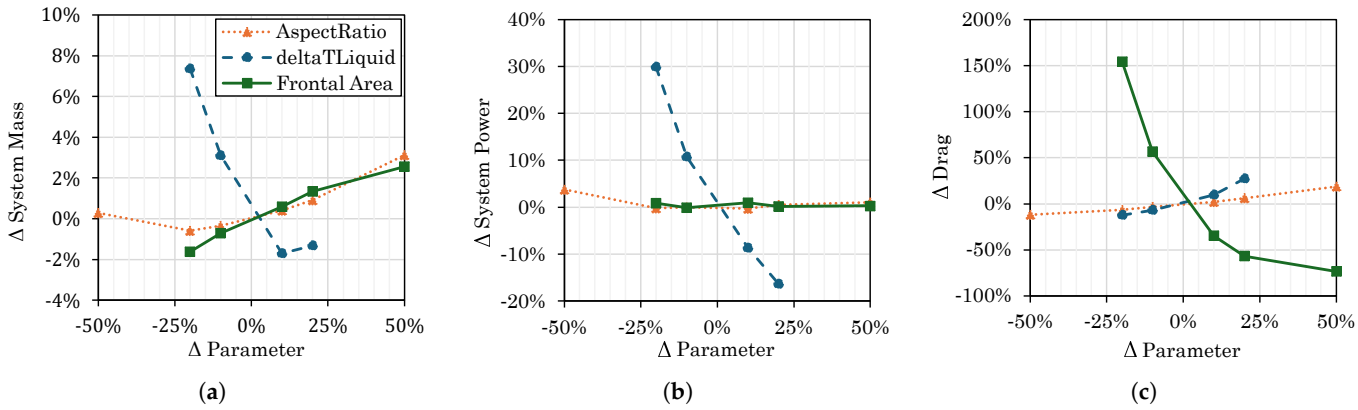



**Figure 11.** Impact of each design variable on (**a**) system mass, (**b**) system power and (**c**) system drag compared to a generic reference.

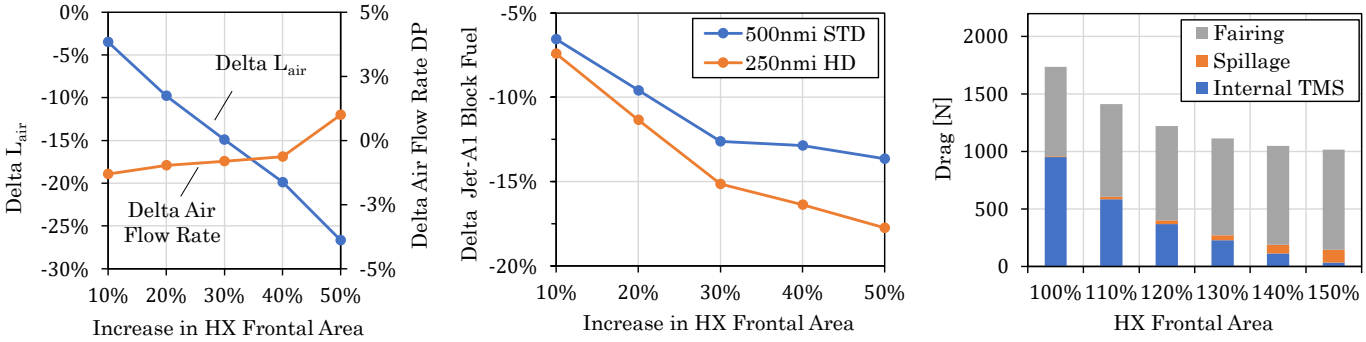
### *5.5. Trade-Off: Heat Exchanger Frontal Area*

This trade-off explores the step-wise increase in heat exchanger frontal area versus the baseline size while keeping the other design parameters of the system constant. This also means that the inlet throat area grows at the same rate as the frontal area. For each heat exchanger frontal area the effectiveness i.e., the air mass flow rate is optimized for lowest impact as discussed in Section 4.9. The optimal air mass flow rate stays almost constant while the air flow length is reduced to match the required heat transfer as shown in Figure 12a. This enables the minimum momentum drag in the design point. This approach stands in contrast to the fixed heat exchanger length imposed by Niehuis et al. [29]. There the air mass flow rate decreases with increasing frontal area leading to higher effectivenesses.

Figure 12b shows the achieved reduction in the Jet-A1 fuel consumption with increasing frontal area for the standard-day mission and the "hot-day" evaluation mission with reduced range at constant maximum payload. Up to 13.6% fuel reduction is achievable on a standard day and 17% on a hot-day with a 50% increase in frontal area. This is also the maximum possible reduction for the standard day.

The reason for this minimum is shown in Figure 12c where the sum of TMS internal, spillage and fairing drag reaches a plateau at this area. The total TMS drag drops by −85% compared to the baseline. However, the spillage drag increases exponentially with larger frontal areas. At the largest area increase of 50% it makes up 63% of the TMS drag. In addition to that the fairing increases in size and adds further drag. Nevertheless, the fairing drag increases only by 12% versus the baseline and plays a minor role in the trade-off. The fairing height growth is slowed down by the fact that with increasing frontal area the optimized heat exchanger air flow length becomes shorter. The fairing mass increases by 26% versus the baseline which equals barely noticeable 0.2% of take-off mass. On the hot-day mission an even larger heat exchanger would further improve the outcome as indicated in Figure 12b because more air is needed to cool the same heat load. This shifts

the rise in the spillage drag with increasing heat exchanger size. The change in hydrogen consumption on the design mission amounts to less than 1% for the trade-off.




(**a**) (**b**) (**c**)

**Figure 12.** (**a**) Change in optimal air flow length and air mass flow rate in the design point (DP) versus the baseline for a step-wise increase in heat exchanger frontal area. (**b**) Impact on Jet-A1 fuel block fuel consumption for the standard-day design mission and the "hot-day" (ISA + 10 °C) mission with reduced range. (**c**) Drag composition per engine during the standard-day cruise flight. The fairing drag shown equals half of the total fairing drag.

### *5.6. Sensitivity Analysis of Weighting Factors*

The weighting factors for the effectiveness optimization of the heat exchanger were discussed in Section 4.9. In the following, the weighting factors are sampled to analyze the actual mission level outcome. This is done for two of the above heat exchanger frontal area variations. The results are given in Table 6 with the deviations of the design and evaluation mission energy (hot-day) as well as the delta in MTOM. The data indicates that in this case the impact of the effectiveness optimization on mission energy is low with differences smaller than 0.5%. The reason is the limited sensitivity of the penalty objective function to effectiveness and the limited range of applicable designs. Considering the overall level of detail and top-level convergence criteria of the study, this difference is negligible. On the hot-day evaluation mission where TMS drag multiplies, the mass-optimized solution leads to a more noticeable increase of 2.2% energy consumption. However, the little differences among the other samples indicate that *K* values of 1 for both drag and mass are sufficient to select a "good" design. Based on these findings, an additional optimization of these weighting factors in the workflow is therefore not considered worth the computational effort.

**Table 6.** Impact of weighting factors at mission level. The deltas are given with respect to the baseline weighting factors of 0.9 for the drag and 0.8 for the mass impact.

| $K_{Drag}$ | $K_{Mass}$ | Δ Energy Design Mission STD | | Δ Energy 250nmi HD | | Δ MTOM | |
|---|---|---|---|---|---|---|---|
| | | 120% Area | 140% Area | 120% Area | 140% Area | 120% Area | 140% Area |
| 1 | 1 | 0% | 0% | 0% | 0% | 0% | 0% |
| 0.5 | 1 | 0% | −0.2% | 0% | 0% | 0% | −0.1% |
| 0 | 1 | +0.5% | 0.1% | +1.8% | +2.2% | −0.5% | −0.4% |
| 1 | 0 | +0.2% | +0.2% | 0% | +0.1% | 0.1% | 0% |
| 1 | 0.5 | 0% | +0.2% | 0% | 0.1% | 0% | 0% |

### *5.7. Trade-Offs: Fuel Cell Sizing and Fuel Cell Temperature*

A fuel cell system can either be optimized for high efficiency, i.e., high mass or low efficiency, i.e., minimal mass. In the workflow this trade-off is performed via the equivalent stack size. The baseline in this study is configured for minimum mass, i.e., maximum stack

load in the cruise design point. When the stack is "oversized" by 20%, the nominal load is 83%. The increase in stack efficiency due to the oversizing is explained in Appendix A. The installation volume of the fuel cell system is assumed to be unconstrained and to not cause additional wetted areas on the airframe. In the trade-off, the stack was oversized by up to 60% while keeping the frontal area of the heat exchanger constant. Figure 13a shows the impact on block Jet-A1 consumption for the standard-day and hot-day missions. The fuel burn reduction amounts up to 12–14% for a 60% oversizing of the stacks. Additionally, a reduction of up to 10% in hydrogen fuel consumption is achieved due to the more efficient stack operation. This confirms the overall positive effect indicated by several studies [5,6,10,11].

Besides the heat load itself, the operating temperature of the fuel cell is a major driver of TMS impact. To investigate this sensitivity, the coolant temperature was step-wise increased from 80 °C up to 95 °C while keeping the heat exchanger frontal area constant. The operating temperature also impacts the performance of the fuel cell. According to Habrard et al. [8], the humidification of the cell becomes more challenging with increasing temperature, potentially degrading the performance. However, recent developments towards high-performance stacks with peak operating temperatures of up to 100 °C and low humidification constraints indicate significant technology advancements [7]. Similarly to the study performed by Habrard et al. [8], the temperature impact on fuel cell performance is neglected. Only the isolated impact on the thermal management system is evaluated. The impact on fuel consumption is shown in Figure 13b. The reduction in fuel consumption behaves similarly to the stack oversizing effect. The main reason for the benefit in both trade-offs is that the TMS drag drastically decreases. This means that the gas turbine has to provide less shaft power to the propeller to compensate the TMS drag and thus to maintain the required cruise thrust. In addition, the change in hydrogen consumption on the design mission is below one percent since the sizing of the fuel cell is unaffected. Overall the results of the higher fuel cell temperature confirm what is indicated by multiple studies on the topic.

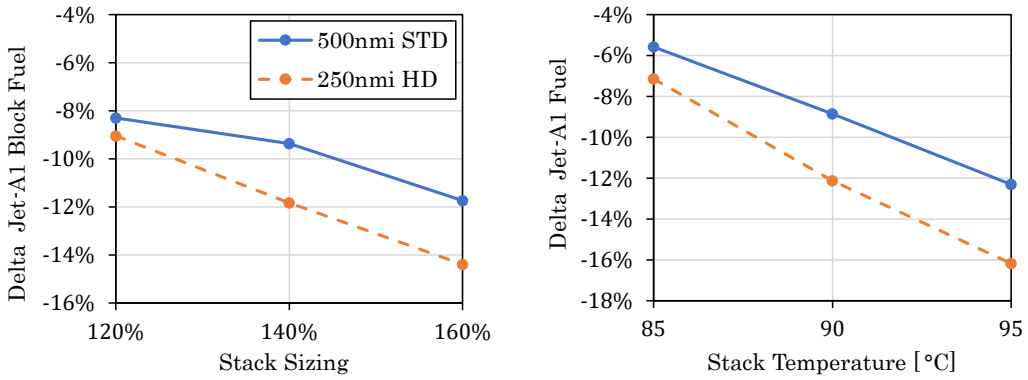



**Figure 13.** Impact on Jet-A1 block fuel consumption for the standard-day design mission and the "hot-day" (ISA + 10 °C) mission with reduced range for an increase in stack sizing in (**a**) and an increase in fuel cell operating temperature in (**b**).

### *5.8. Discussion*

The specific heat rejection, i.e., the ratio of heat rejection to TMS total drag (excluding the fairing drag) of each trade-off is plotted against the baseline value of 1.77 in Figure 14a. A higher specific heat rejection means a lower drag since the drag is the denominator. The frontal area oversizing achieves values more than six times higher compared to the

baseline. This equals a substantial TMS drag reduction of 85%. The temperature and stack oversizing trade-offs achieve roughly three times the specific heat rejection of the baseline. This equals an absolute drag reduction of 63% for the maximum temperature and 74% for the largest stack size.

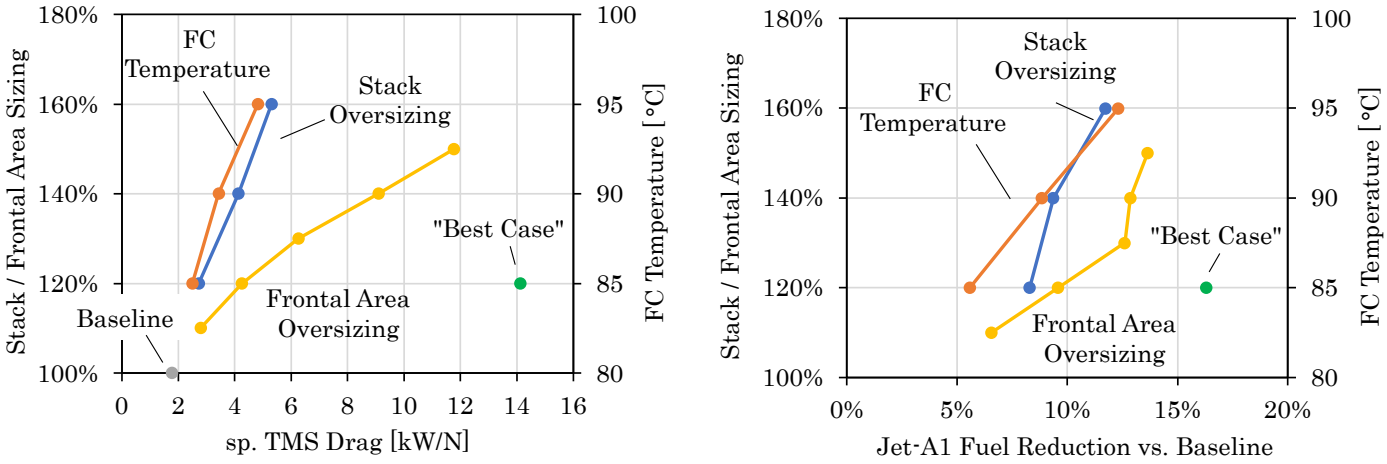



**Figure 14.** (**a**): Drag-specific heat rejection of baseline and stack oversizing, operating temperature and frontal oversizing trade-offs on standard-day cruise flight. (**b**) Impact of each trade-off on Jet-A1 consumption on the standard-day design mission.

Figure 14b shows the total Jet-A1 block fuel reduction of the various trade-offs versus the baseline. All trade-offs achieve double-digit Jet-A1 fuel savings of 10 to 15%. An optimal setup would exploit all available synergies among the trade-offs. For example, the green dot in Figure 14 shows the result of a 120% stack size combined with a 50% increase in frontal area. This combination cuts the TMS drag by 89% versus the baseline. The sizing methodology benefits this combination of fuel cell and heat exchanger size implicitly. This leads to less drag at a slightly higher hybridization ratio, giving a further reduction in Jet-A1 fuel consumption. In this case the drag is dominated by the spillage effect.

Overall, the increased frontal area leads to major benefits that outperform the penalty of larger fairings. The larger fairings turn out to not penalize the aircraft as much because they seamlessly extend the space already required by the landing gear fairing. However, this circumstance is specific to the aircraft configuration and the fuel cell and thermal management system integration.

The study is idealized in several aspects. For one, in the sense that irregular interference drag penalties between the cooling air entering or exiting the fairing and the fuselage are assumed to be dealt with by a subsequent detailed design of the aircraft. The diffusor pressure drop estimation in the trade-offs is based on the best-case scenario with respect to inlet blockage. Furthermore, losses due to heat exchanger tilting and ducting losses downstream of the heat exchanger are neglected. Therefore, the prediction is considered rather optimistic. However, in the case of the above trade-offs concerning the absolute figures, this might be offset by the fact that the baseline heat exchanger geometry itself as the biggest impact driver is a conservative starting point. Using for example the geometry configuration 90 (see Sections 5.2 and 5.3) would lead to a considerable shift in all the trade-offs towards less TMS impact. After all, a full characterization of the opposed effects and their impact is outside the scope of the present work.

## 6. Conclusions and Outlook

An aircraft design workflow was set up to investigate the impact of a ram-air fuel cell thermal management system on the fuel economy of a twin-turboprop aircraft equipped with a parallel-hybrid propulsion system. The penalties of internal and external drag, system mass and power consumption are considered in the aircraft design process. Various thermal management system design parameters were investigated in sensitivity studies. The impact ranking on fuel and energy consumption in descending order is summarized as follows:

1. **Fin geometry of the heat exchanger:** Small variations in the geometric definition of the air passage and the tube diameter show the largest sensitivities in terms of pressure drop and thus impact. This shows the optimization potential but also introduces an uncertainty in the model.
2. **Heat exchanger frontal area:** This design parameter largely drives the impact of a heat exchanger with a given fin geometry. Large areas are always recommended if the aircraft integration permits it.
3. **Liquid coolant temperature drop:** Variations in reasonable boundaries show moderate impact. However, this parameter is not unconstrained as it is linked to the heat source.
4. **Heat exchanger aspect ratio:** This parameter helps to optimize the space allocation on the airframe but has little impact on internal drag, power consumption or system mass.

The thermal management system impact is inherently connected to the sizing of the fuel cell. The oversizing of the fuel cell stacks towards higher efficiency proved to be a useful measure to reduce the impact. The benefits of higher fuel cell operating temperatures towards drag reduction were confirmed.

This trade-off showed that the total thermal management system impact can be manageable even with low-performing heat exchanger internal geometries and low operating temperatures if it is possible to integrate a large heat exchanger with limited impact on external drag.

The findings show the wide-ranging impact of fuel cell thermal management on this specific aircraft concept. Optimized louver-fin cores or other types of heat exchanger geometries should be considered to lower the pressure drop at a given frontal area and to facilitate the aircraft integration.

Future work should be directed at a more specific and detailed analysis to improve the performance prediction. Such an analysis should include a review of the heat exchanger placement in the duct, its sensitivity to internal pressure losses and also the characterization of the external flow around the landing gear fairing.

**Author Contributions:** Conceptualization, P.B., D.S. and T.B.; Methodology, D.S., P.B., T.B. and A.G.M.; Software, D.S. and P.B.; Validation, D.S., T.B. and P.B.; Investigation: P.B.; Resources, D.S., P.B. and T.B.; Writing, P.B. and T.B. All authors have read and agreed to the published version of the manuscript.

**Funding:** This research was funded by the European Union, under Grant Agreement Number 101102008. Views and opinions expressed are, however, those of the author(s) only and do not necessarily reflect those of the European Union or Clean Aviation Joint Undertaking. Neither the European Union nor Clean Aviation JU can be held responsible for them.

**Data Availability Statement:** The original contributions presented in this study are included in the article. Further inquiries can be directed to the corresponding author.

**Conflicts of Interest:** The authors declare no conflicts of interest. The funders had no role in the design of the study; in the collection, analyses, or interpretation of data; in the writing of the manuscript; or in the decision to publish the results.

## Nomenclature

The following nomenclature is applied in this manuscript:

**Abbreviations**

| | |
|---|---|
| AC | Alternating Current |
| CPACS | Common Parametric Aircraft Configuration Schema |
| DLR | German Aerospace Center |
| DM | Design Mission |
| FC | Fuel Cell |
| GT | Gas Turbine |
| HHV | Higher Heating Value |
| HD | Hot Day |
| HX | Heat Exchanger |
| ISA | International Standard Atmosphere |
| KTAS | Knots True Airspeed |
| LDG | Landing Gear |
| LHV | Lower Heating Value |
| LT | Low Temperature |
| MTOM | Maximum Take-off Mass |
| MW | Mega Watt |
| NACA | National Advisory Committee for Aeronautics |
| OEM | Operating Empty Mass |
| PEM | Polymer Electrolyte Membrane |
| STD | ISA Standard Day |
| TMS | Thermal Management System |
| TLAR | Top-Level Aircraft Requirement |
| TOFL | Take-off Field Length |

**Roman Symbols**

| | | |
|---|---|---|
| $A$ | Area | $m^2$ |
| $A_0$ | Free-flow area | $m^2$ |
| $AR_{Dif}$ | Diffusor area ratio | - |
| $AR_{HX}$ | Heat exchanger aspect ratio | - |
| $C$ | Absolute heat capacity | W/K |
| $C_f$ | Friction coefficient | - |
| $c_p$ | Specific heat capacity at constant pressure | J/(kgK) |
| $C^*$ | Ratio of absolute heat capacities | - |
| $CD$ | Drag coefficient | - |
| $d_h$ | Hydraulic diameter | m |
| $D$ | Drag | N |
| $f$ | Friction factor | - |
| $F_p$ | Fin pitch | mm |
| $FF$ | Form factor | - |
| $G_c$ | Mass velocity | $kg/(m^2s)$ |
| $I$ | Stack current | A |
| $j$ | Colburn factor | - |
| $j/f$ | Area goodness factor | |
| $K_{add}$ | Multiplier on additive drag | - |
| $K_{Drag}$ | Weighting factor for drag impact | - |
| $K_{Power}$ | Weighting factor for power impact | - |
| $K_{Mass}$ | Weighting factor for mass impact | - |

| | | |
|---|---|---|
| $K_c$ | Compression coefficient | - |
| $K_e$ | Expansion coefficient | - |
| $k$ | Thermal conductivity | W/(mK) |
| $L$ | Length | m |
| $m$ | Mass | kg |
| $\dot{m}$ | Mass flow rate | kg/s |
| $MFR$ | Mass flow ratio ($A_\infty/A_{in}$) | - |
| $N_{air}$ | Air side number of transfer units | - |
| $N_{liq}$ | Liquid side number of transfer units | - |
| $NTU$ | Overall number of transfer units | - |
| $p$ | Pressure | Pa |
| $P$ | Power | W |
| $q$ | Dynamic pressure $\rho/2v^2$ | Pa |
| $\dot{Q}$ | Heat flow rate | W |
| $Q$ | Interference factor | - |
| $Re$ | Reynolds number | - |
| $SP$ | Specific power | kW/kg |
| $T$ | Temperature | K |
| $T_p$ | Tube pitch | mm |
| $T_d$ | Tube diameter | mm |
| $U$ | Overall heat transfer coefficient | W/(m$^2$K) |
| $v$ | Velocity | m/s |
| $\dot{V}$ | Volume flow rate | m$^3$/s |
| **Greek Symbols** | | |
| $\alpha$ | Heat transfer coefficient | W/(m$^2$K) |
| $\gamma$ | Heat exchanger tilt angle | ° |
| $\delta$ | Fin thickness | mm |
| $\epsilon$ | Heat exchanger effectiveness | - |
| $\eta_0$ | Surface efficiency | - |
| $\eta_f$ | Fin efficiency | - |
| $\eta_p$ | Pump efficiency | - |
| $\mu_f$ | Fuel utilization ratio | - |
| $\rho$ | Density | kg/m$^3$ |
| $\Phi$ | Normalized TMS penalty | - |
| **Subscripts** | | |
| $air$ | Air side | |
| $d$ | Design | |
| $liq$ | Liquid side | |
| $fric$ | Friction | |
| $HX$ | Heat exchanger | |
| $m$ | Mean | |
| $min$ | Minimum | |
| $st$ | Stack | |
| $sys$ | Auxiliary fuel cell systems | |

## Appendix A. Fuel Cell Model

The relationship of the stack efficiency versus the power output depends on the polarization curve of a stack. A qualitative picture of a polarization curve is given in Figure A1a. The decrease in voltage with rising current is modelled only for the near linear region extending on the left to a minimum of 5% power. The efficiency of a stack can be modelled as

$$\eta_{st} = \mu_f \cdot \frac{U_{st}}{E_0}, \tag{A1}$$

where $\mu_f$ is the fuel utilization coefficient with an assumed value of 0.95 and $E_0$ = 1.25 V, which is the electric equivalent if all chemical energy were transformed into electricity based on the lower heating value (LHV) [45]. The reference data of the polarization curve of a state-of-the-art fuel cell is taken from Schröder et al. [5]. The resulting efficiency is then extrapolated with a technology factor of 10% increase (see Figure A1b). The electric power drawn from the fuel cell stack is

$$P_{st} = U_{st} \cdot I. \tag{A2}$$

Two data points are used to define the linear relationship in the model (69% efficiency at 20% power and 56% efficiency at 100% rated power). This is similar to the efficiency at maximum rated power that is estimated in the FAME project for EIS in 2040 [46]. A linear model is also used by similar aircraft design studies [46,47]. It is not considered a standard for fuel cells. However, it is based on test data and is sufficiently accurate for the aircraft conceptual design stage. The hydrogen fuel flow is calculated via

$$\dot{m}_{H2} = \frac{P_{st}}{\eta_{st} \cdot LHV}. \tag{A3}$$

The stack can be oversized at its design point with a design load factor to a lower nominal working point according to

$$P_{st,max} = P_{st} / f_{designLoad}. \tag{A4}$$

This enables the trade-off between mass and efficiency. The total stack mass is computed via

$$m_{st} = P_{st,max} / SP_{st}, \tag{A5}$$

where $SP_{st}$ is the stack specific power at the rated power of a reference stack, neglecting the effect of finite cells per stack. The stack power therefore equals a stack assembly's power consisting of multiple stacks per module. The stack specific power is set at 5 kW/kg and the specific volume at 5 kW/l based on project targets.

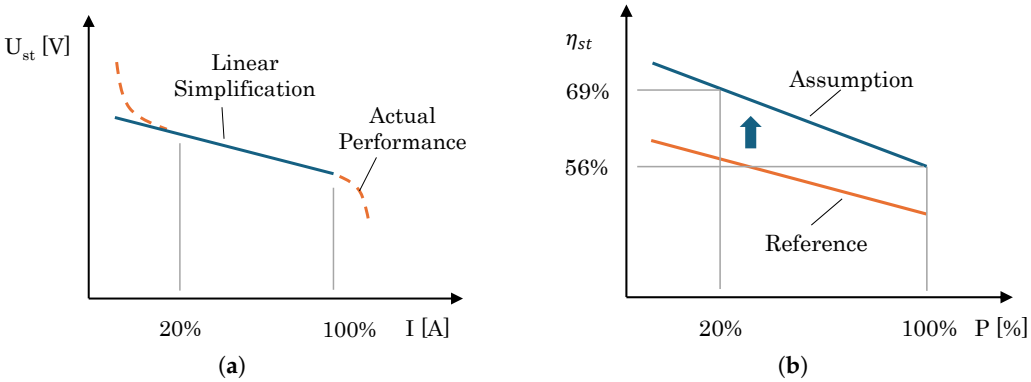



**Figure A1.** (**a**) Qualitative polarization curve with linear range (**b**) Relationship between stack efficiency and relative power output.

The power consumed by the balance of plant (i.e., compressor, pumps) is modelled with a fixed consumption ratio dependent on altitude and regardless of load. The net system power is then

$$P_{net} = P_{st} \cdot (1 - f_{BoP}(alt)), \tag{A6}$$

with $f_{BoP}$ as the power ratio ranging from 8% at sea level to 19% at cruise. These values are derived from the fuel cell design study performed by Schröder et al. [5]. The mass of the auxiliary systems is computed by

$$m_{sys} = P_{sys}/SP_{sys}, \tag{A7}$$

with $SP_{sys}$ as the ratio of electrical input power to system mass. The waste heat to be removed by the coolant is computed as

$$\dot{Q}_{st} = P_{st} \cdot (\frac{1}{\eta_{st}} - 1) \cdot \frac{HHV}{LHV} \cdot (1 - f_{exhaustHeat}). \tag{A8}$$

This equation is an approximation based on the complete heat balance given by Schröder et al. [5]. Computing the heat only from the LHV efficiency would underestimate the heat generation. Therefore the ratio $HHV/LHV$ and the term $(1 - f_{exhaustHeat})$ are introduced. The exhaust acts as a heat sink in terms of sensible cathode and anode flow heating. Furthermore, the latent heat of water vaporization absorbs some of the generated heat. These three heat sinks are represented by the reduction factor $f_{exhaustHeat}$. However, in the present work, a conservative approach was taken and $f_{exhaustHeat}$ was set to zero.

## Appendix B. Heat Transfer Model

The liquid side number of transfer units

$$N_{liq} = 4L_{liq}\frac{j_{liq}}{d_{h,liq}Pr_{liq}^{\frac{2}{3}}}, \tag{A9}$$

depends on the liquid side flow length $L_{liq}$, the Colburn factor $j_{liq}$ and the liquid Prandtl number

$$Pr_{liq} = \left(c_{p_m}\rho_m\frac{\nu_m}{k_f}\right)_{liq}. \tag{A10}$$

The properties of specific heat capacity $c_{p_m}$, density $\rho_m$, viscosity $\nu_m$ and thermal conductivity $k_f$ are evaluated for the liquid coolant at the mean temperature which is assumed to be the arithmetic mean. The hydraulic diameter per unit cell is defined according to [35] as

$$d_h = 4L\frac{A_0}{A}, \tag{A11}$$

where $L$ is the respective flow length, $A_0$ the free-flow area and $A$ the wetted surface. The Reynolds number

$$Re_{liq} = \frac{v_{liq}d_{h,liq}}{\nu_{liq}}, \tag{A12}$$

is required for the determination of the Colburn factor according to [35] as

$$j_{liq} = \frac{Nu_{liq}}{Re_{liq}Pr_{liq}^{\frac{1}{3}}}. \tag{A13}$$

The liquid side Nusselt number $Nu_{liq}$ is determined with the methods for heat transfer in pipe flow (chapter G1) from [37]. Transforming Equation (15), the number of air side transfer units

$$N_{air} = \frac{C_{min}}{C_{air}}\frac{1}{NTU^{-1} - \frac{C_{min}}{C_{liq}}\frac{1}{N_{liq}}} \tag{A14}$$

is computed. According to [35] the air side length can be estimated

$$L_{air} = d_{h,air} Pr_{air}^{\frac{2}{3}} \frac{N_{air}}{4 j_{air}} \frac{1}{\eta_0}. \tag{A15}$$

The surface effectiveness of the air side is determined via

$$\eta_0 = 1 - (1 - \eta_f) \left( \frac{A_f}{A} \right)_{cell} \tag{A16}$$

as presented in [36]. The fin efficiency is determined based on [36] from

$$\eta_f = \frac{\tanh(ml)}{ml}, \tag{A17}$$

$$ml = \sqrt{2 \frac{\alpha}{k_f \delta} (1 + \frac{\delta}{L_f})} \left( \frac{L_f}{2} - \delta \right). \tag{A18}$$

with the fin thickness $\delta$ and the fin length $L_f$ defined in Equation (A24). The thermal conductivity of the aluminum fins $k_f$ is set to 237 W/(mK). The air side heat transfer coefficient $\alpha$ is estimated as

$$\alpha = \frac{Nu_{air} \cdot k_{air}}{d_{h,air}}. \tag{A19}$$

The mean temperatures relevant for the physical flow properties in the heat exchanger core are computed as follows:

$$T_{air_m} = T_{liq_m} - \Delta T_m, \tag{A20}$$

$$\Delta T_m = \frac{(T_{liq_m} - T_{air_{out}}) - (T_{liq_m} - T_{air_{in}})}{\ln \left( \frac{T_{liq_m} - T_{air_{out}}}{T_{liq_m} - T_{air_{in}}} \right)}, \tag{A21}$$

$$T_{liq_m} = \frac{T_{liq_{in}} + T_{liq_{out}}}{2}. \tag{A22}$$

This approach is valid for heat capacity ratios $C^* < 0.5$ [36], which was confirmed for the configurations and application cases in this study. The mean air density is computed according to [36] as

$$\rho_{air_m} = \frac{2}{\frac{1}{\rho_{in}} + \frac{1}{\rho_{out}}}. \tag{A23}$$

## Appendix C. Core Geometry Considerations

The determination of the air side cell and total areas is based on the formulas found in Shah (8.76–8.82) [36]. The free-flow area of the cell is multiplied with a calibration factor of 0.95 to account for braze fillets. This gives more realistic results of the porosity in the range of 85% to 95% (excluding the blockage of the tubes). The primary surface area on the air side includes the area blocked by the tube on the front and rear side as suggested by Shah et. al. [36]. It is assumed that, primarily for this reason, that the computed hydraulic diameter according to Equation (A11) is slightly smaller compared to what is stated in the database in [39]. The rectangular channel type C is treated in the same way as the triangular channel shape of type A because of minor differences in surface areas and fin efficiencies. The fin length is computed as

$$L_f = T_p - T_d. \tag{A24}$$

The tube wall thickness is estimated at a minimum of 0.2 mm and a maximum of 10% of the tube diameter.

The passage arrangement is assumed to always have a hot passage enclosed by two cold passages (i.e., C-H-C…C-H-C), in line with the assumption of Schröder et al. [5]. It is also assumed that the outer two cold layers then have a fin length half that of the inner cold passages in order to be symmetrical. Furthermore, there are top and bottom end plates as well as side bars considered to seal the air passages. These plates are assumed to have a thickness of 1 mm. This additional mass is accounted for in the mass method.

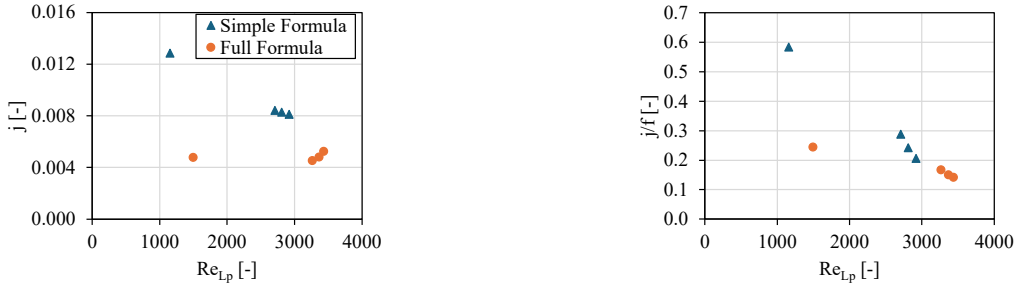
Table A1 lists the selected internal heat exchanger geometry which is based on the configuration 89 from Chang et al. [39].

**Table A1.** Baseline internal heat exchanger geometry (based on Chang configuration 89).

| Parameter | Value |
|---|---|
| Tube pitch | 11.1 mm |
| Tube diameter | 1.5 mm |
| Fin pitch | 1.8 mm |
| Fin thickness | 0.15 mm |
| Louver pitch | 1.1 mm |
| Louver angle | 25.5° |
| Louver length | 6.8 mm |

## Appendix D. Sensitivity Study on Heat Transfer Correlation

Chang et al. provide a short (Equation (A2) in [39]) and an expanded heat transfer correlation (Equation (9) in [39]) for estimation of the non-dimensional Colburn factor. As discussed earlier, the short or simple one is only sensitive to the louver pitch Reynolds number, while the full correlation also considers a lot of geometric dependencies. According to Chang et al. the simple one is intended for "very quick evaluation of heat transfer coefficient in an engineering application" [39]. It is clear that in any case the preferred correlation is the extended one as it covers many more nuances in the HX geometry. Nonetheless, it helps to understand the impact of geometric parameters. Figure A2 shows four different geometries from the Chang database and their results with respect to the Colburn factor $j$ in (a) and the so-called 'area goodness factor' $j/f$, the ratio of $j$ to the Fanning friction factor $f$ in (b). Each configuration is optimized in terms of effectiveness according to the normalized approach. For this reason, the Reynolds number between the simple and full $j$ correlations does not remain constant. Based on the simple formula, one would try to optimize for the shortest louver pitch to achieve the highest $j/f$. However, as expected, the extended formula "levels" a lot of the nuances among the configurations. This leads to a lower scatter of the data also for the goodness factor $j/f$. The extended formula estimates double-digit reductions in $j$ and $j/f$. The simple formula can thus be regarded as also more optimistic.




(**a**) (**b**)

**Figure A2.** (**a**) Colburn factor for the simple and the full correlation from Chang. (**b**) Goodness factor j/f for the simple and the full Colburn correlation from Chang.

## Appendix E. Liquid Side Pressure Drop

The estimation of the friction factor $f$ is based on four different regimes: The laminar, the transitional, the turbulent with lower Reynolds numbers and the turbulent with higher Reynolds numbers. According to [37], the usage of an equivalent hydraulic diameter for the estimation of the friction factor for a flat tube is acceptable. The coolant pressure drop in the heat exchanger is estimated by

$$\Delta p_{HX} = \frac{\rho}{2} v^2 \frac{4 L_{liq}}{D_{h_{liq}}} f_{fric} \tag{A25}$$

and the pressure drop in the pipe by

$$\Delta p_{HX} = \frac{\rho}{2} v^2 \frac{4 L_{pipe} \cdot 2.5}{D_{h_{pipe}}} f_{fric}. \tag{A26}$$

The pipe length $L_{pipe}$ is the roughly estimated distance between the stacks and the heat exchanger. A margin of 50% length is added on top to account for turns required for integration. In the laminar regime up to Re <= 2300, the Hagen–Poiseuille relationship is used to estimate the friction factor

$$f_{fric} = \frac{1}{4} \frac{64}{Re}. \tag{A27}$$

In the turbulent regime for hydraulically smooth pipes with Reynolds numbers up to $10^5$ the friction factor

$$f_{fric} = \frac{1}{4} \frac{0.3164}{Re^{0.25}}. \tag{A28}$$

is estimated based on the Blasius relationship according to [41] et al.

For Reynolds numbers in the transitional regime between 2300 and 4000, a linear interpolation between Hagen–Poiseuille and Blasius in line with [5] is used. For Reynolds numbers above $10^5$, the correlation from Nikuradse for hydraulic smooth pipes is used as provided in [41]

$$f_{fric} = \frac{1}{4} \left( 0.0032 + \frac{0.221}{Re^{0.237}} \right) \tag{A29}$$

## Appendix F. Pump Weight Estimation

The pump weight estimation relationships of various studies are given in Table A2. The one from Quaium et al. is based on datasheets published by the Ebara company. The exact type of pump is not stated. It is assumed that those pumps are not optimized for lightweight aerospace applications. The correlation from Link et al. is based on datasheets from main aircraft fuel pumps from the Eaton company and fuel pumps of the Parker company at flow rates up to 10 l/s. It was found that the Eaton main fuel pumps can deliver pressure increases of around 10 bar, which is considered overpowered for the application case. This might explain the high mass compared to the other correlations. Link et al. also see potential for lower pump masses based on data from automotive water pumps [48].

An example calculation for the use case in the present study is shown in Table A3. The correlations from Quaium et al. and Link et al. estimate the highest masses. This was expected as the technical background does not fit the application. They were used for MW-level systems composed of multiple fuel cell blocks with several hundred kW of power. The correlation from van Gerner et al. is based on an automotive water coolant pump. It fits the application and the required pressure increase and it was used for MW-level studies. Schröder et al. used a baseline aviation pump and scaled it via the mass flow for a 300 kW fuel cell system. The selected pump is the Eaton type 7100 engine feed boost pump with

a rated mass flow of 5 kg/s. This pump is an AC-driven pump and therefore requires a motor controller. This was not considered, which partially explains why it is the lightest in the comparison. The correlation was based on an operating point that delivers a pressure rise of 0.8 bar. However, the scaling law quickly rises two orders of magnitude when a pressure increase of 2 bar is required for this type of pump. Not only the fuel flow but also the pressure increase drives the mass of a pump. Ideally, both are aligned with the requirements of the intended application. The Eaton company produces various types of aircraft fuel pumps. It was found that the Eaton AC-driven jettison pump type 39 delivers the required pressure rise of 2 bar for 12 kg/s at a comparably low weight [49]. This pump baseline mass and a specific power assumption of 5 kW/kg for the motor controller were assumed as an alternative, linear scaling law for the present study. The present correlation gives a mass below the one from van Gerner et al. and is thus considered optimistic. However, it is assumed that aerospace pumps could be lighter than automotive pumps because of other priorities in the development. Nevertheless, it is acknowledged that the Eaton jettison pump is not an ideal baseline for this application. Further research on applicable scaling laws is recommended to establish a mass estimation method that covers the required pressure rise and volume flow of a MW-level cooling loop. Water coolant pumps from large, state-of-the-art aviation piston engines might provide reasonable data points for such analysis.

**Table A2.** Overview of weight estimation relationships for the pump.

| WER [kg] | Units | Source | Used Cooling Range/Scaling Baseline |
|---|---|---|---|
| $0.0308 \cdot P_{pump} + 1.1912$ | $P_{pump}$ in W | Quaium et al. [3] | 400 kW/- |
| $3.2941 \cdot \dot{V} + 3.0944$ | $\dot{V}$ in l/s | Link et al. [48] | 300 kW/10 l/s |
| $1.368 \cdot \dot{V} + 0.3864$ | $\dot{V}$ in l/s | van Gerner et al. [7] | MW level/- |
| $0.68 \cdot \dot{m}$ | $\dot{m}$ in kg/s | Schröder et al. [5] | 300 kW/5 kg/s |
| $0.84 \cdot \dot{m} + P_{pump}/5$ | $\dot{m}$ in kg/s, $P_{pump}$ in kW | Present Study | MW level/12 kg/s |

**Table A3.** Example for the pump mass estimation. The assumed coolant mass flow is 38 kg/s , i.e., a volume flow of 36.9 l/s and a pump power of 15 kW.

| Pump Mass [kg] | Source |
|---|---|
| 463 | Quaium et al. [3] |
| 125 | Link et al. [48] |
| 51 | van Gerner et al. [7] |
| 26 | Schröder et al. [5] |
| 35 | Present Correlation |

## References

1. Atanasov, G.; Silberhorn, D. (2025): EXACT Sustainable Aircraft Concepts Results and Comparison. Deutsche Gesellschaft für Luft- und Raumfahrt - Lilienthal-Oberth e.V. (Text). Available online: https://publikationen.dglr.de/?tx_dglrpublications_pi1%5bdocument_id%5d=630388 (accessed on 14 October 2026).
2. Aerospace Technology Institute. *Zero-Carbon Emission Aircraft Concepts: FZO-AIN-REP-0007*; Aerospace Technology Institute: London, UK, 2022
3. Quaium, F.; Bielsky, T.; Thielecke, F. (2024): Fuel Cell Cooling System Design for Hydrogen-Powered Concept Aircraft. Deutsche Gesellschaft für Luft- und Raumfahrt - Lilienthal-Oberth e.V. (Text). Available online: https://publikationen.dglr.de/?tx_dglrpublications_pi1%5bdocument_id%5d=570127 (accessed on 14 October 2026).

4. Sain, C.K.; Hänsel, J.; Kazula, S. Preliminary Design of Air and Thermal Management of a Nacelle-Integrated Fuel Cell System for an Electric Regional Aircraft. In Proceedings of the IEEE Transportation Electrification Conference & Expo (ITEC), Detroit, MI, USA, 21–23 June 2023. [CrossRef]
5. Schröder, M.; Becker, F.; Gentner, C. Optimal design of proton exchange membrane fuel cell systems for regional aircraft. *Energy Convers. Manag.* **2024**, *308*, 118338. [CrossRef]
6. Schmelcher, M.; Häßy, J. Hydrogen fuel cells for aviation? A potential analysis comparing different thrust categories. In Proceedings of the ISABE Conference, Ottawa, ON, Canada, 25–30 September 2022.
7. van Gerner, H.J.; Luten, T.; Resende, W.; Mühlthaler, G.; Buntz, M.B. System Analysis and Comparison Between a 2 MW Conventional Liquid Cooling System and a Novel Two-Phase Cooling System for Fuel Cell-Powered Aircraft. *Energies* **2025**, *18*, 849. [CrossRef]
8. Habrard, V.; Pommier-Budinger, V.; Hazyuk, I.; Jézégou, J.; Benard, E. Parametric Study of a Liquid Cooling Thermal Management System for Hybrid Fuel Cell Aircraft. *Aerospace* **2025**, *12*, 377. [CrossRef]
9. Filipe, M.; Afonso, F.; Suleman, A. A Study on Thermal Management Systems for Fuel-Cell Powered Regional Aircraft. *Energies* **2025**, *18*, 3074. [CrossRef]
10. Rischmüller, U.C.J.; Lessis, A.; Egerer, P.; Hornung, M. Conceptual Design of a Hydrogen-Hybrid Dual-Fuel Regional Aircraft Retrofit. *Aerospace* **2024**, *11*, 123. [CrossRef]
11. Massaro, M.C.; Pramotton, S.; Marocco, P.; Monteverde, A.H.A.; Santarelli, M. Optimal design of a hydrogen-powered fuel cell system for aircraft applications. *Energy Convers. Manag.* **2024**, *306*, 118266. [CrossRef]
12. H2GEAR hydrogen aircraft project for UK. *Fuel Cells Bull.* **2021**, *2021*, 6. [CrossRef]
13. Nozinski, M.; Meyer, P.; Delony, F.; Friedrichs, J.; Göing, J.; Kabelac, S. On the Design and Operation of the Thermal Management System of PEMFC-Powered Aircraft. *Aerospace* **2026**, *13*, 243. [CrossRef]
14. Eissele, J.; Lafer, S.; Mejía Burbano, C.; Schließus, J.; Wiedmann, T.; Mangold, J.; Strohmayer, A. Hydrogen-Powered Aviation—Design of a Hybrid-Electric Regional Aircraft for Entry into Service in 2040. *Aerospace* **2023**, *10*, 277. [CrossRef]
15. Nicolosi, F.; Melone, G.; Di Stasio, M. Impact of Thermal Management System Design on Aircraft Performance in Hydrogen Fuel Cell Powertrains. In Proceedings of the AIAA SCITECH 2026 Forum, Reston, VA, USA, 12–16 January 2026. [CrossRef]
16. Clean Aviation Hybrid-Electric Regional Architecture Project (HERA). 2025. Available online: https://project-hera.eu/home (accessed on 20 February 2026).
17. Wöhler, S.; Atanasov, G.; Silberhorn, D.; Fröhler, B.; Zill, T. Preliminary Aircraft Design within a Multidisciplinary and Multifidelity Design Environment. In Proceedings of the Aerospace Europe Conference, Bordeaux, France, 25–28 February 2020.
18. Bräunling, W.J. *Flugzeugtriebwerke*; Springer: Berlin/Heidelberg, Germany, 2015. [CrossRef]
19. Boden, B.; Flink, J.; Först, N.; Mischke, R.; Schaffert, K.; Weinert, A.; Wohlan, A.; Schreiber, A. RCE: An Integration Environment for Engineering and Science. *SoftwareX* **2021**, *15*, 100759. [CrossRef]
20. Alder, M.; Moerland, E.; Jepsen, J.; Nagel, B. Recent Advances in Establishing a Common Language for Aircraft Design with CPACS. In Proceedings of the Aerospace Europe Conference, Bordeaux, France, 25–28 February 2020.
21. Fröhler, B.; Hesse, C.; Atanasov, G.; Wassink, P. (2021): Disciplinary Sub-Processes to Assess Low-Speed Performance and Noise Characteristics within an Aircraft Design Environment. Deutsche Gesellschaft für Luft- und Raumfahrt - Lilienthal-Oberth e.V. (Text). Available online: https://publikationen.dglr.de/?tx_dglrpublications_pi1%5bdocument_id%5d=530201 (accessed on 14 October 2026).
22. Burschyk, T.; Hämisch, J.; Villada Quiceno, V. Liquid Hydrogn Fuel System: Architecture and Modelling Approach. In Proceedings of the Architecting Future Aviation Symposium, Hamburg, Germany, 1–2 April 2025.
23. Leachman, J.W.; Jacobsen, R.T.; Penoncello, S.G.; Lemmon, E.W. Fundamental Equations of State for Parahydrogen, Normal Hydrogen, and Orthohydrogen. *J. Phys. Chem. Ref. Data* **2009**, *38*, 721–748. [CrossRef]
24. Nichols, M. *Investigation of Flow Through an Intercooler Set at Various Angles to the Supply Duct: NACA-WR-L-408*; NACA: Washington, DC, USA, 1942. Available online: https://ntrs.nasa.gov/citations/19930093676 (accessed on 14 October 2026).
25. Torenbeek, E. *Advanced Aircraft Design*; John Wiley & Sons: Hoboken, NJ, USA, 2013. [CrossRef]
26. Siggel, M.; Kleinert, J.; Stollenwerk, T.; Meierl, R. An Open Source Computational Geometry Library for Parametric Aircraft Design. *Math. Comput. Sci.* **2019**, *13*, 367–389. [CrossRef]
27. Torenbeek, E. *Synthesis of Subsonic Airplane Design*; Springer: Dordrecht, The Netherlands, 1982. [CrossRef]
28. Chapman, J.W.; Schnulo, S.L.; Nitzsche, M.P. Development of a Thermal Management System for Electrified Aircraft. In Proceedings of the AIAA Scitech Forum, Orlando, FL, USA, 6–10 January 2020. [CrossRef]
29. Niehuis, M.; Jeschke, P. Performance Calculation of the Thermal Management System for a Fuel Cell Aircraft Engine. In Proceedings of the GPPS Technical Conference, Chania, Greece, 4–6 September 2024. [CrossRef]
30. Kozulovic, D. Heat Release of Fuel Cell Powered Aircraft. In Proceedings of the GPPS Chania20, Online, 7–9 September 2020. [CrossRef]

31. Kellermann, H.; Lüdemann, M.; Pohl, M.; Hornung, M. Design and Optimization of Ram Air–Based Thermal Management Systems for Hybrid-Electric Aircraft. *Aerospace* **2021**, *8*, 3. [CrossRef]
32. Pittaluga, F. A set of correlations proposed for diffuser performance prediction. *Mech. Res. Commun.* **1981**, *8*, 161–168. [CrossRef]
33. Malan, P.; Brown, E.F. Inlet drag prediction for aircraft conceptual design. *J. Aircr.* **1994**, *31*, 616–622. [CrossRef]
34. Mount, J.S. Effect of inlet additive drag on aircraft performance. *J. Aircr.* **1965**, *2*, 374–378. [CrossRef]
35. Hesselgreaves, J.E.; Law, R.; Reay, D.A. *Compact Heat Exchangers: Selection, Design and Operation*; Butterworth-Heinemann: Oxford, UK, 2016.
36. Shah, R.K.; Sekulić, D.P. *Fundamentals of Heat Exchanger Design*; John Wiley & Sons: Hoboken, NJ, USA, 2003.
37. Gesellschaft Verfahrenstechnik und Chemieingenieurwesen (VDI-GVC). *VDI Heat Atlas*, 2nd ed.; Springer Reference; Springer: Berlin/Heidelberg, Germany, 2010. [CrossRef]
38. BASF SE. *Glysantin FC G 20-00/50: Coolant For Fuel Cells*; TI/ES 1656 e; BASF SE: Ludwigshafen, Germany, 2006.
39. Chang, Y.J.; Wang, C.C. A generalized heat transfer correlation for Iouver fin geometry. *Int. J. Heat Mass Transf.* **1997**, *40*, 533–544. [CrossRef]
40. Chang, Y.J.; Hsu, K.C.; Lin, Y.T.; Wang, C.C. A generalized friction correlation for louver fin geometry. *Int. J. Heat Mass Transf.* **2000**, *43*, 2237–2243. [CrossRef]
41. Grote, K.H.; Bender, B.; Göhlich, D. (Eds.) *Dubbel—Taschenbuch für den Maschinenbau*, 25th ed.; Neu Bearbeitete und Aktualisierte Auflage; Springer: Berlin, Germany, 2018.
42. Frey, A.C.; Stonham, J.; Bosak, D.; Sangan, C.M.; Pountney, O.J. Radiators in fuel cell powered aircraft: The effect of heat rejection on drag. *Appl. Therm. Eng.* **2025**, *274*, 126697. [CrossRef]
43. *AS18802*; Fuel and Oil Lines, Aircraft, Installation of: AS18802. SAE International: Warrendale, PA, USA, 1998.
44. German Aerospace Center. *Press Release: Zero-Emission Air Transport—First Flight of Four-Seat Passenger Aircraft*; German Aerospace Center: Cologne, Germany, 2016. Available online: https://www.dlr.de/en/latest/news/2016/20160929_zero-emission-air-transport-first-flight-of-four-seat-passenger-aircraft-hy4_19469 (accessed on 14 October 2026).
45. Donateo, T. Semi-Empirical Models for Stack and Balance of Plant in Closed-Cathode Fuel Cell Systems for Aviation. *Energies* **2023**, *16*, 7676. [CrossRef]
46. Di Stasio, M.; Cusati, V.; Nicolosi, F.; Melone, G. Propagation of Hydrogen-Subsystem Characteristics to Aircraft Level in a Liquid-Hydrogen Fuel-Cell Short-Range Aircraft. *Hydrogen* **2026**, *7*, 120. [CrossRef]
47. Schlittenhardt, J.; Freund, Y.; Mangold, J.; Hanke-Rauschenbach, R.; Strohmayer, A. Preliminary Design of Regional Aircraft—Integration of a Fuel Cell-Electric Energy Network in SUAVE. *Aerospace* **2025**, *12*, 249. [CrossRef]
48. Link, A.; Staggat, M.; DeGraaf, S. Characterisation of thermal management specific heat rejection for electric propulsion architectures. In Proceedings of the Aerospace Europe Conference, Lausanne, Switzerland, 10–13 July 2023. [CrossRef]
49. Eaton Aerospace Limited. *Override/Jettison Pump and Canister: 39-0002 Boost Pump, Form No. DS600-121A*; Eaton Aerospace Limited: Hampshire, UK, 2013.


**Disclaimer/Publisher's Note:** The statements, opinions and data contained in all publications are solely those of the individual author(s) and contributor(s) and not of MDPI and/or the editor(s). MDPI and/or the editor(s) disclaim responsibility for any injury to people or property resulting from any ideas, methods, instructions or products referred to in the content.